The Influence of Heat Transport on Arctic Amplification

by

Laura Elizabeth Fleming

B.S., Northeastern University, 2014

Submitted in partial fulfillment of the requirements for the degree of

Master of Science

at the

MASSACHUSETTS INSTITUTE OF TECHNOLOGY

and the

WOODS HOLE OCEANOGRAPHIC INSTITUTION

February 2019

Author .....
Joint Program in Oceanography/Applied Ocean Science and Engineering
Massachusetts Institute of Technology
and Woods Hole Oceanographic Institution
January 18, 2019

Certified by .....
Young-Oh Kwon
Senior Scientist
Woods Hole Oceanographic Institution
Thesis Supervisor

Accepted by .....
Glenn Flierl
Chair, Joint Committee for Physical Oceanography
Massachusetts Institute of Technology/
Woods Hole Oceanographic Institution

The Influence of Heat Transport on Arctic Amplification

by

Laura Elizabeth Fleming

Submitted to the Joint Program in Oceanography/Applied Ocean Science and Engineering
Massachusetts Institute of Technology
and Woods Hole Oceanographic Institution
on January 18, 2019, in partial fulfillment of the
requirements for the degree of
Master of Science

Abstract

The Arctic surface air temperature has warmed nearly twice as much as the global mean since the mid-20th century. Arctic sea ice has also been declining rapidly in recent decades. There is still discussion about how much of this Arctic amplification is caused by local factors, such as changes in surface albedo, versus remote factors, such as changes in heat transport from the midlatitudes. This thesis focuses mainly on the role of poleward heat transport on Arctic amplification. Most of the previous studies on this topic have defined ocean heat transport as the zonally averaged ocean heat transport at 65°N or 70°N, which ignores the physical pathways of heat into the Arctic and may include recirculation of heat in the North Atlantic. In this thesis, we define the ocean heat transport as the heat transport across five sections surrounding the Arctic, to create a closed domain in the Arctic.

Previous studies on Arctic amplification have used either a single model run or have compared results from a multi-model ensemble. While the multi-model ensemble approach may potentially average out biases in individual models, the ensemble spread confounds the model differences and the internal climate variability. In this thesis, we investigate the Arctic amplification in the Community Earth System Model version 1 (CESM1) Large Ensemble. The CESM1 Large Ensemble includes 40 members that use the same model and external forcing, but different initializations. This simulates different climate trajectories that can occur in a given atmosphere-ocean-land-cryosphere system.

We find that CESM1 Large Ensemble projects a large increase towards the end of the 21st century in ocean heat transport into the Arctic, and that the increase in ocean heat transport is significantly correlated with Arctic amplification. The main contributor to the increase in ocean heat transport is the increase across the Barents Sea Opening. The increase in Barents Sea Opening ocean heat transport is highly correlated with the decrease in sea ice in the Barents-Kara Sea region. We propose that this is because the increase in ocean heat transport melts the ice at the sea ice margin, which results in increased surface heat flux from the ocean and further local feedback through decreased surface albedo and increased cloud coverage. We also find that while the changes in atmosphere heat transport into the Arctic circle at 66.5°N are on the same order as the changes in ocean heat transport, they are not correlated with Arctic amplification.

Thesis Supervisor: Young-Oh Kwon
Title: Senior Scientist
Woods Hole Oceanographic Institution

Acknowledgments

Most of all, I would like to thank Young-Oh Kwon. I would not have finished this thesis without your support over the years. Thank you for teaching me how to be a scientist. Thank you for always believing in me, even though I often doubted myself. You were the best, kindest, most supportive advisor I could have asked for.

I would also like to thank Jake Gebbie for acting as my interim advisor for the past year. It was great to have a new perspective on research. Again, I would not have been able to finish this thesis without your help and guidance. I would also like to thank Claudia Cenedese, Raffaele Ferrari, and Paul O'Gorman for their feedback on my research. I'd like to thank Nicolas Barrier for his help with updating PyPAGO for CESM.

I would like to thank my colleagues in the Joint Program, particularly Suzi Clark, Jake Forsyth, Mara Freilich, and Joleen Heiderich. I'm so grateful that you all were available for help, laughter, commiseration, and interpretive dance sessions.

I am so grateful for the love and support of my family. Thank you for always being there for me. Finally, I'd like to thank my partner, Joe. You are always willing to listen when I am stuck on a problem. You have done so much to support me and cheer me on. I am so grateful that you are in my life, and I can't wait for our next big adventure.

Contents

List of Figures

List of Tables

Chapter 1

Introduction

The Arctic surface air temperature has warmed nearly twice as much as the global mean since the mid-20th century, a characteristic known as Arctic amplification. Arctic warming is strongest during the fall and weakest during the summer. Warming is strongest at the surface but it extends throughout the troposphere [Cohen, 2018]. There have also been concurrent reductions in sea ice cover. A record low sea ice extent was observed in 2007 and again in 2012 [Comiso et al., 2008, Cohen, 2018]. The monthly mean summer sea ice extent has decreased $86,000$ km^2 per year, or 13.3% per decade, between 1979 and 2014 [Serreze and Stroeve, 2015]. The mechanisms of Arctic amplification can be categorized into two groups: local processes and remote forcing. Local processes includes greenhouse gas increase, cloud cover change, albedo changes, lapse rate feedback, and changes in surface heat fluxes from the Arctic Ocean. Remote forcing includes changes in poleward heat and moisture transport from lower latitudes.

Past studies have investigated the relationship between Arctic amplification and sea ice changes. The surface albedo in the Arctic ranges from ~ 0.8 for ice that is at least 1 meter thick, to ~ 0.1 for open ocean [Hall, 2004, Perovich et al., 2007]. This reduction in sea ice increases the absorbance of solar radiation. Removing ice cover also increases the surface turbulent flux between the ocean and the atmosphere, which then induces increased downward longwave radiation due to cloud feedback. Surface warming is closely linked to diminishing sea ice cover between 1989–2006 [Screen and Simmonds, 2010]. Similarly, Screen et al. [2012] showed that local sea ice concentration (SIC) changes and local sea surface temperature (SST) changes explain most of the Arctic air temperature warming based on

simulations using atmospheric general circulation models. In the Coupled Model Intercomparison Project Phase 3 (CMIP3) simulations, Arctic amplification is strongly correlated with surface albedo changes [Hwang et al., 2011]. However, Arctic amplification can also occur in models without changes in sea ice [Alexeev et al., 2005].

For accurate long-term sea ice predictions, models need accurate representations of the heat transport into the Arctic from the midlatitudes. If climate models are initialized with accurate ocean data, and therefore have accurate heat transport anomalies, they produce skillful predictions of sea ice extent on decadal time scales [Yeager et al., 2015]. Similarly, accurate representations of Atlantic ocean heat transport, Pacific ocean heat transport, and the Arctic dipole may be necessary for accurate decadal projections in Arctic sea ice changes [Zhang, 2015]. These results suggest that remote factors influence Arctic amplification.

Under global warming, the amount of heat transported to the Arctic by the atmosphere may change. The atmosphere heat transport (AHT) can be decomposed in a few different ways: (1) transient and stationary wave components, (2) large-scale planetary waves and synoptic-scale waves dominated by meso-scale cyclones, or (3) dry static energy and latent energy transports. For example, Graversen and Burtu [2016] showed that the Arctic is much more affected by AHT due to planetary waves than synoptic-scale waves. Other studies showed that the latent energy transport has a greater impact on the Arctic temperature variability than the dry static energy component [Graversen et al., 2011, Kapsch et al., 2013]. Under global warming scenarios, the warmer atmosphere can hold more moisture, which leads to an increase in latent energy transport. However, this decreases the equator-to-pole temperature gradient, which decreases the dry static energy transport. This compensation is seen in both energy balance models [Hwang and Frierson, 2010] and general circulation models [Hwang and Frierson, 2010, Hwang et al., 2011]. As such, CMIP3 models with high Arctic amplification tend to have the smallest increases, or even decreases, in AHT into the Arctic. Some studies (e.g. Graversen et al. [2008], Hwang et al. [2011], Yoshimori et al. [2017]) calculate the atmosphere heat transport directly from the moist static energy flux. Other studies (e.g Hwang and Frierson [2010], Feldl et al. [2017]) calculate AHT from the difference between top-of-the-atmosphere net radiative flux and surface fluxes, including radiative, latent heat, and sensible heat fluxes. However, if there is an imbalance between the incoming and outgoing solar radiation, the imbalance will accumulate. This will result in a non-zero northward heat transport at the North Pole, which is physically impossible.

Furthermore, the heat transport cannot be divided into the components from latent energy and dry static energy. In this thesis, we calculate AHT directly from the velocity and moist static energy. This provides the best possible estimate of the AHT.

Ocean heat transport (OHT) could also play a role in Arctic amplification. General circulation models, including the Coupled Model Intercomparison Projects Phase 3 (CMIP3) and Phase 5 (CMIP5) models, show an increase in ocean heat transport into the Arctic under global warming scenarios [Hwang et al., 2011, Nummelin et al., 2017]. One proposed mechanism for this is that in the sub-polar region, the atmosphere warms faster than the ocean under global warming, so the ocean loses less heat to the atmosphere. This allows an increase in OHT into the Arctic, driving an increase in the ocean heat content of the Arctic Ocean [Nummelin et al., 2017]. However, models with larger increases in OHT tend to have larger decreases in AHT, so the total change in heat transport is small [Held and Soden, 2006, Hwang et al., 2011].

Although there have been previous studies on how OHT is related to Arctic amplification, the methods of calculating OHT have often not been ideal. For example, Hwang et al. [2011] calculated the OHT implied from the surface heat fluxes, because not many models in the CMIP3 archive provided a zonally integrated northward OHT directly calculated from the ocean velocity and temperature. One problem with using the indirect method is that the change in ocean heat content needs to be estimated. Most studies ignore the change in ocean heat content, and thus practically assume the change is negligible. Singh et al. [2017] included an ocean heat content storage term for the mixed layer, but ignored the deeper ocean. However, on decadal or longer time scales, the change in the deeper ocean heat content may be significant. If one assumes that changes in ocean heat content are negligible, then the surface fluxes need to be in balance or there will be an accumulation of error at the poles. If this is not the case, the surface fluxes might need to be adjusted in some way. On the other hand, Nummelin et al. [2017] used the monthly mean zonally integrated northward ocean heat transport from the CMIP5 models, which are directly calculated using the ocean velocity and temperature. Similarly, Oldenburg et al. [2018] used the zonally integrated northward OHT, calculated from ocean velocity and temperature data. As we will show in this thesis, the trend in the zonally integrated northward OHT is very sensitive to the choice of latitude. In this thesis, we calculate the OHT across the various straits that lead directly into the Arctic. This provides a better representation of the amount of heat that actually

enters the Arctic.

Previous studies have often ignored the effect of the internal variability of the climate system, and therefore may have obfuscated the signal of the external forcing. Generally, there are three sources of uncertainty in the projections of future climate using climate models: choice of emissions-scenario forcing, model-dependent response uncertainty, and internal natural variability [Hawkins and Sutton, 2009, Deser et al., 2012]. The first can be examined by using a variety of emission-scenarios. The second can be examined by using multiple models from independent research groups, such as the multi-model ensemble approach of CMIP3 and CMIP5. The third can only be researched using many ensemble members from the same climate model, so called a large ensemble approach. For the large ensemble of a single model, each ensemble member is subject to the same external forcing conditions but has different initial conditions. Then the differences in the ensemble members is not due to the changes in external forcing or inter-model variability, but only the internal variability of the model's climate system. For example, September Arctic sea ice extent (SIE) trends during 2020–2059 range from -2×10^6 to -5.7×10^6 km^2 in a 39-member ensemble of the Community Climate System Model, version 3 (CCSM3) [Wettstein and Deser, 2014]. The large range in SIE trend can only be attributed to the interval variability of the model's climate. Different variables can exhibit different sensitivities to internal variability. Screen et al. [2014] used large ensembles from the UK-Australian Unified Model (UM) version 7.3 and the US National Center for Atmospheric Research (NCAR) Community Atmosphere Model (CAM) version 3 to separate the forced response from atmospheric internal variability in Arctic sea ice loss. They showed that the forced response of temperature and precipitation to the external forcing is significantly easier to detect than the forced response of sea level pressure or geopotential height. The sea level pressure and geopotential height have low signal-to-noise ratios, and the forced response is masked by the atmospheric internal variability.

Overall, this thesis addresses several shortcomings with previous research. The first is that it calculates the OHT directly from the temperature and velocity, at the straits that lead directly to the Arctic. This ensures that the OHT calculation is as accurate as possible. It also ensures that we are only considering the heat that actually enters the Arctic, and not heat that is recirculated back southward. The second improvement is that we include data from 40 ensemble members from one model. With only one ensemble member, it is impossible

to disentangle the effects of external forcing from the effects of internal variability. In theory, the differences caused by internal variability will cancel when many ensemble members are averaged together. The ensemble mean then represents the model's response to the external forcing. Furthermore, the ensemble spread is used to accurately estimate the range of the internal variability, thus the signal-to-noise ratio for the externally forced signal, and also to clearly attribute the degree of Arctic amplification to the varying strength of the OHT into the Arctic.

This thesis is organized as follows: Chapter 2 describes the models used in this study. Chapter 3 defines Arctic amplification and investigates the spatial characteristics within the models. Chapter 4 describes the atmosphere heat transport in the models, and explores the relationship between AHT and Arctic amplification. Chapter 5 examines the ocean heat transport into the Arctic, and examines the link between OHT and Arctic amplification. Finally, Chapter 6 summarizes this thesis.

Chapter 2

Models

The primary dataset used in this study is the Community Earth System Model version 1 (CESM1) Large Ensemble [Kay et al., 2015]. CESM1 consists of coupled atmosphere, ocean, sea ice, and land components. For the atmosphere, the CESM1 Large Ensemble uses the Community Atmosphere Model, version 5 (CAM5) with a finite volume dynamical core at 1 degree horizontal resolution. For the ocean, it uses the Parallel Ocean Program, version 2 (POP2) model, with a displaced grid with nominally 1 degree horizontal resolution. The atmosphere and ocean have 30 and 60 vertical levels, respectively.

The first ensemble member was initialized from 1850 with constant pre-industrial radiative forcing. The atmosphere, land, and sea ice processes were initialized from previous CESM1 simulations. The ocean was initialized from a state of rest using modern observations from the Polar Science Center Hydrographic Climatology (PHC2) potential temperature and salinity data. This dataset merges the World Ocean Atlas [Antonov, 1998] with the regional Arctic Ocean Atlas [Environmental Working Group (EWG), 1997]. This ensemble member was run until it reached quasi-equilibrium with the pre-industrial forcing, and then run from 1850–2100. The model used historical forcing from 1850–2005, and representative concentration pathway 8.5 (RCP8.5) forcing [Meinshausen et al., 2011, Lamarque et al., 2011] from 2005–2100.

The remaining ensemble members were initialized from the first ensemble member. A temperature perturbation on the order of 10^{-14} K was added to the air temperature field on January 1, 1920 for each member. Although the ensemble members start with nearly identical temperatures, they diverge within a few weeks (Figure 2-1, black lines). Members

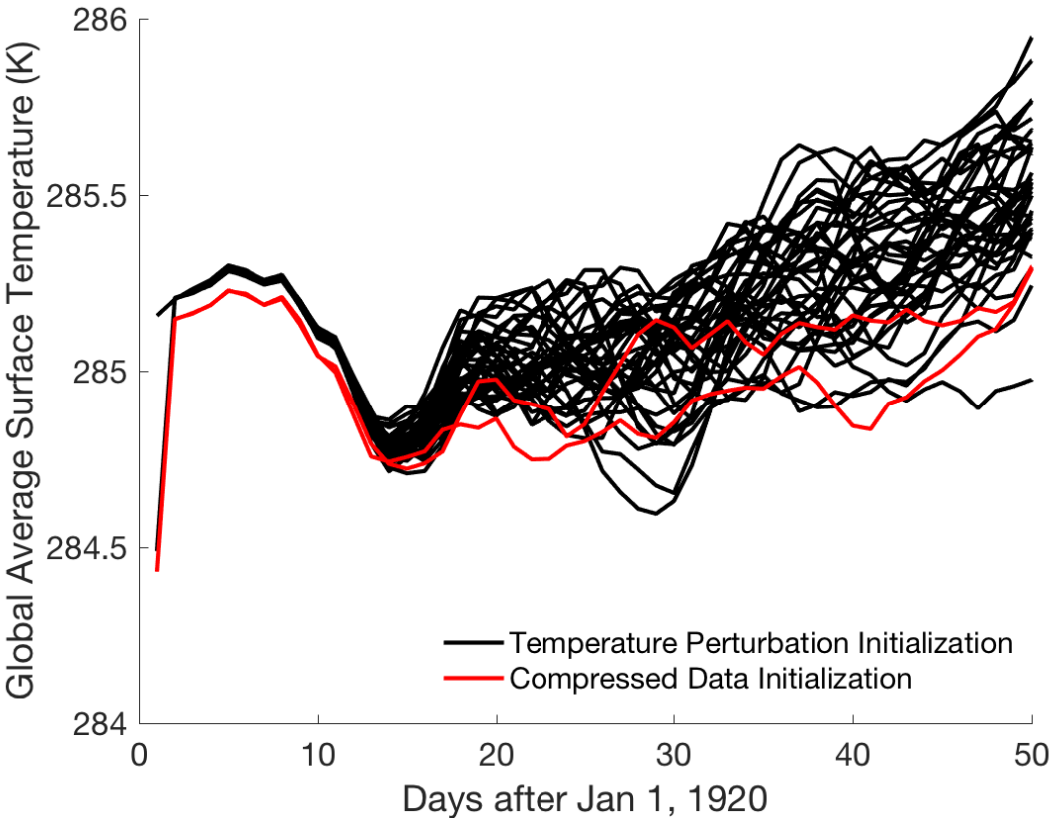

Figure 2-1: Globally averaged daily mean surface temperature for the CESM1 Large Ensemble. The black lines indicate the ensemble members that were initialized by adding a temperature perturbation to ensemble member 1. The red lines indicate the models initialized using compressed data.

31 and 33 were initialized with compressed data from ensemble member 1 [Baker et al., 2014]. This increases the initial perturbation on the ensemble member, which resulted in lower global temperature initially (Figure 2-1, red lines). After a few weeks, the results from the compressed initial conditions fall within the natural variability of the uncompressed initial conditions [Baker et al., 2014].

The ensemble members were then run from 1920–2100. All have the same historical forcing for 1920–2005 and RCP8.5 forcing for 2005–2100. Each ensemble member exemplifies a different state that the atmosphere could be in, given the external forcing and initial condition. Because all ensemble members have the same initial ocean conditions, and because the ocean has a much longer time scale compared to the atmosphere, the CESM1 Large Ensemble does not show a sampling of significantly different ocean states until the 1940s. Since the ensemble members have identical external forcing, the difference between the en-

semble members is only due to the internal variability, or "climate noise." [Screen et al., 2014]. With enough ensemble members, it is possible to separate the model's response to the external forcing from this climate noise.

Even though the focus of this research is on the forced response of the CESM1 model to global warming, it is still important to look at the CESM1 Large Ensemble in the context of other climate models. For this reason, we also use models from the Coupled Model Intercomparison Project Phase 5 (CMIP5). The CMIP5 models include pre-industrial, historical, and future simulations from various modeling groups [Taylor et al., 2012]. We compare the results from the CESM1 Large Ensemble to those from CMIP5 when possible. Table 2.1 lists the 35 CMIP5 models used in this study. These models all include simulations for historical and RCP8.5 forcing. Models were only included if they had all of the variables used in this study.

Model Name	**Model Group**
ACCESS1-0	Commonwealth Scientific and Industrial Research Organization (CSIRO) and Bureau of Meteorology (BOM), Australia
ACCESS1-3	Commonwealth Scientific and Industrial Research Organization (CSIRO) and Bureau of Meteorology (BOM), Australia
bcc-csm1-1	Beijing Climate Center, China Meteorological Administration
bcc-csm1-1-m	Beijing Climate Center, China Meteorological Administration
CanESM2	Canadian Centre for Climate Modelling and Analysis
CCSM4	National Center for Atmospheric Research
CESM1-BGC	Community Earth System Model Contributors
CESM1-CAM5	Community Earth System Model Contributors
CMCC-CESM1	Centro Euro-Mediterraneo per I Cambiamenti Climatici
CMCC-CM	Centro Euro-Mediterraneo per I Cambiamenti Climatici
CMCC-CMS	Centro Euro-Mediterraneo per I Cambiamenti Climatici
CNRM-CM5	Centre National de Recherches Météorologiques / Centre Européen de Recherche et Formation Avancée en Calcul Scientifique
CSIRO-Mk3-6-0	Commonwealth Scientific and Industrial Research Organization in collaboration with Queensland Climate Change Centre of Excellence
FGOALS-g2	LASG, Institute of Atmospheric Physics, Chinese Academy of Sciences and and CESS, Tsinghua University

Model Name	**Model Group**
GFDL-CM3	NOAA Geophysical Fluid Dynamics Laboratory
GFDL-ESM2G	NOAA Geophysical Fluid Dynamics Laboratory
GFDL-ESM2M	NOAA Geophysical Fluid Dynamics Laboratory
GISS-E2-H	NASA Goddard Institute for Space Studies
GISS-E2-H-CC	NASA Goddard Institute for Space Studies
GISS-E2-R	NASA Goddard Institute for Space Studies
GISS-E2-R-CC	NASA Goddard Institute for Space Studies
HadGEM2-AO	National Institute of Meteorological Research / Korea Meteorological Administration
HadGEM2-CC	Met Office Hadley Centre (additional HadGEM2-ES realizations contributed by Instituto Nacional de Pesquisas Espaciais)
HadGEM2-ES	Met Office Hadley Centre (additional HadGEM2-ES realizations contributed by Instituto Nacional de Pesquisas Espaciais)
inmcm4	Institute for Numerical Mathematics
IPSL-CM5A-LR	Institut Pierre-Simon Laplace
IPSL-CM5A-MR	Institut Pierre-Simon Laplace
IPSL-CM5B-LR	Institut Pierre-Simon Laplace
MIROC-ESM	Japan Agency for Marine-Earth Science and Technology, Atmosphere and Ocean Research Institute (The University of Tokyo), and National Institute for Environmental Studies

Model Name	**Model Group**
MIROC-ESM-CHEM	Japan Agency for Marine-Earth Science and Technology, Atmosphere and Ocean Research Institute (The University of Tokyo), and National Institute for Environmental Studies
MIROC5	Atmosphere and Ocean Research Institute (The University of Tokyo), National Institute for Environmental Studies, and Japan Agency for Marine-Earth Science and Technology
MPI-ESM-LR	Max-Planck-Institut für Meteorologie (Max Planck Institute for Meteorology)
MPI-ESM-MR	Max-Planck-Institut für Meteorologie (Max Planck Institute for Meteorology)
MRI-CGCM3	Meteorological Research Institute
NorESM1-M	Norwegian Climate Centre

Table 2.1: Models and modeling centers for CMIP5 data used in this thesis.

Chapter 3

Arctic Amplification

We define Arctic amplification as the ratio between the area-weighted average warming north of 66.5°N and the area-weighted average global warming,

$$AA = \frac{\Delta T_{arctic}}{\Delta T_{global}} \tag{3.1}$$

where T is the near-surface air temperature. For this analysis, we compare the average temperature from 2001-2020 to the average temperature from 2081–2100.

All CESM1 Large Ensemble members show stronger warming in the Arctic than in the global mean (Figure 3-1), which results in an Arctic amplification of $AA = 2.54 \pm 0.07$ in the CESM1 Large Ensemble. Similarly, the CMIP5 models also show stronger Arctic warming than global warming, with an Arctic amplification of $AA = 2.34 \pm 0.31$. As expected, the CMIP5 multi-model ensemble exhibits a larger spread than the CESM1 Large Ensemble members. This is because the spread in the CMIP5 ensemble includes both the uncertainty due to model-dependent response and the uncertainty due to natural variability in each model's climate. Meanwhile, the spread in the CESM1 Large Ensemble only demonstrates uncertainty due to natural variability. While the CESM1 Large Ensemble Arctic amplification is well within the range of values of the CMIP5 models, the two mean values are significantly different at 5% based on the pooled two-sample Student's t-test. This is caused by both the differences in the change in Arctic temperatures and the change in global temperatures. Student's t-test rejects the null hypothesis that the CESM1 ΔT_{arctic} and the CMIP5 ΔT_{arctic} are samples from Gaussian distributions with equal mean and equal variance at the 5% level. Similarly, Student's t-test rejects that the CESM1 ΔT_{global} and

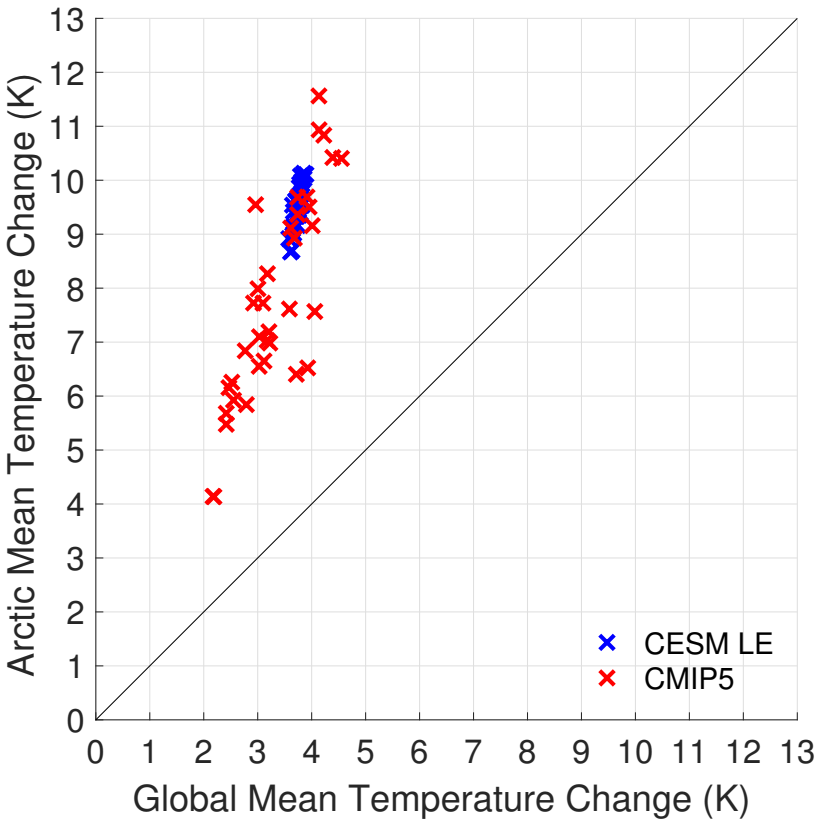

Figure 3-1: Scatter plot of the change in Arctic temperatures versus global temperatures between 2001–2020 and 2081–2100 for the CESM1 Large Ensemble (blue) and CMIP5 (red).

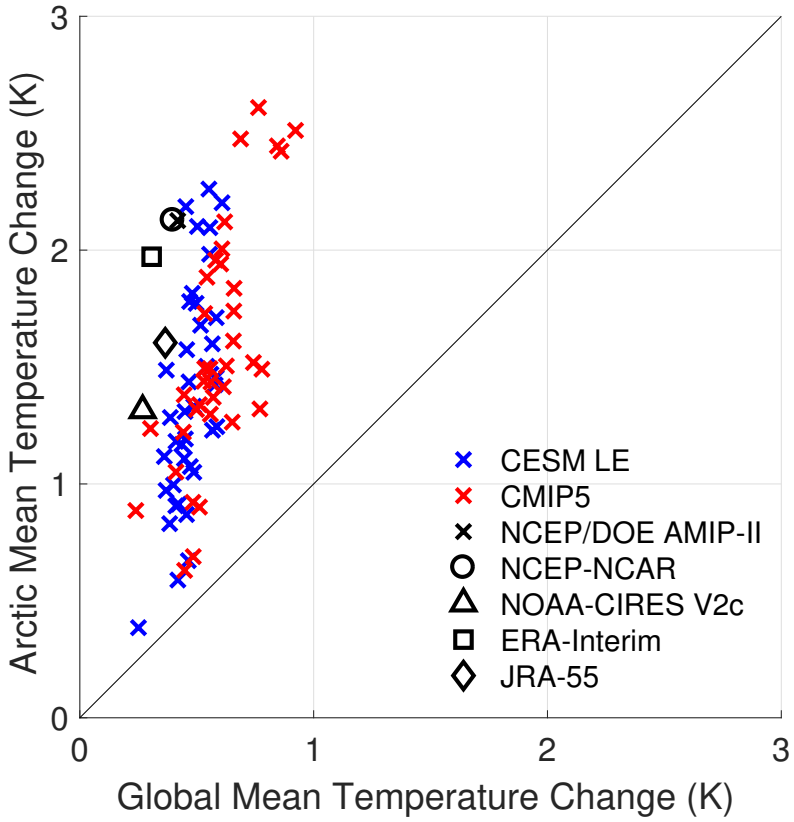

Figure 3-2: Scatter plot of the change in Arctic temperatures versus global temperatures between 1980–1989 and 2005–2014 for the CESM1 Large Ensemble (blue), CMIP5 (red), and reanalyses (black).

the CMIP5 ΔT_{global} are samples from Gaussian distributions with equal mean and equal variance at the 5% level.

We compared these results to that of five reanalysis datasets: NCEP/DOE AMIP-II Reanalysis Model [Kanamitsu et al., 2002], NCEP-NCAR Reanalysis 1 [Kalnay et al., 1996], NOAA-CIRES 20th Century Reanalysis (V2c) [Compo et al., 2011], ERA-Interim [Dee et al., 2011], and the Japanese 55-year Reanalysis (JRA-55) [Kobayashi et al., 2015]. These reanalyses provide global coverage of near-surface air temperature. For the reanalyses, we analyze the change in temperature between the time periods 1980–1989 and 2005–2014. In this shorter time span, we expect a greater influence of the internal climate variability in decadal to multi-decadal time scales. All five reanalyses show that the Arctic warmed more in this time period than the global average (Figure 3-2), with a mean Arctic amplification of 5.22, with a range from 4.39 to 6.42. During this time period, CESM1 Large Ensemble has a mean Arctic amplification of $AA = 2.86 \pm 0.79$, and CMIP5 has a mean Arctic amplification of $AA = 2.68 \pm 0.64$.

In the CESM1 Large Ensemble, the ensemble mean temperature is increasing almost uniformly throughout the Arctic (Figure 3-3a). The largest spread in the temperature change is found over the Barents Sea (Figure 3-3b). There is also enhanced spread north of the Bering Strait. The CMIP5 ensemble mean also shows a more or less uniform increase in temperature throughout the Arctic (Figure 3-4a). However, the amplitude of the mean change is smaller, which is consistent with the respective values of Arctic amplification. CMIP5 exhibits greater spread in the temperature trends than CESM1 Large Ensemble (Figure 3-4b), and the variability is no longer localized to Barents Sea. Instead, generally everywhere in the Arctic, especially in the interior of the Arctic, has a large spread between the models.

Spatial pattern of the sea ice change suggests the surface air temperature change in the Arctic is closely related to the sea ice change. The overall region of the enhanced surface temperature warming closely matches with the region delineated by the sea ice margin. Although there is sea ice loss everywhere in the Arctic, there is enhanced sea ice loss in the Barents Sea and in Chukchi-Beaufort Seas in the CESM1 Large Ensemble (Figure 3-5a). The highest spread in sea ice loss among the ensemble members is near the sea ice margin in Barents Sea (Figure 3-5b). In addition, an enhanced spread is also found near the ice margin in the Chukchi Sea. These two regions of enhanced ensemble spread of sea ice loss

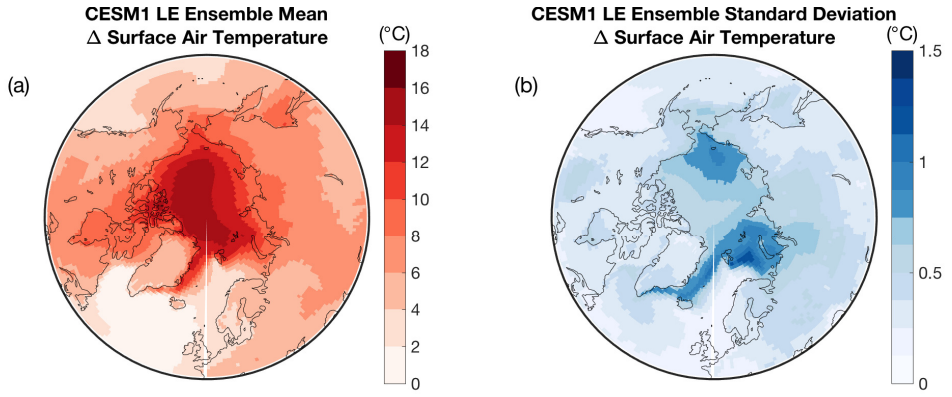

Figure 3-3: Ensemble mean (a) and standard deviation (b) for change in surface air temperature between 2001–2020 and 2081–2100 for the CESM1 Large Ensemble.

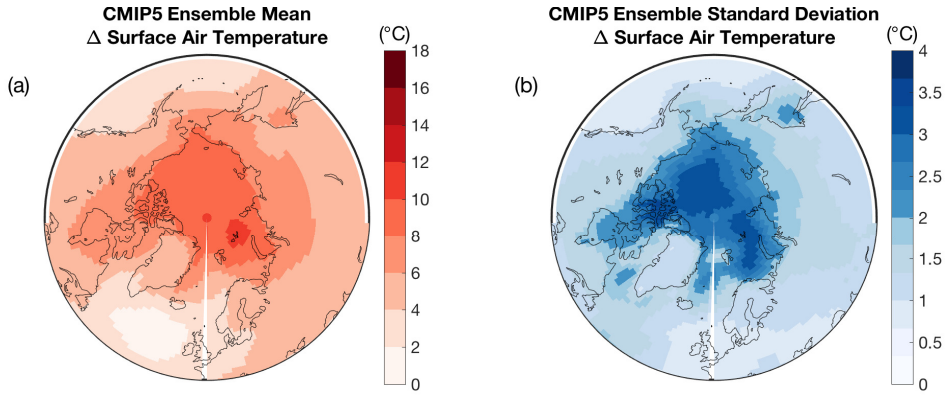

Figure 3-4: Ensemble mean (a) and standard deviation (b) for change in surface air temperature between 2001–2020 and 2081–2100 for CMIP5.

coincide with the regions of enhanced ensemble spread in the near-surface air temperature. This relationship demonstrates the link between the Arctic amplification and the sea ice loss. In CMIP5, the maximum sea ice loss is found in the same general regions, although the sea ice loss is more uniform throughout the Arctic (Figure 3-6a). The ensemble spread in CMIP5 is also much more uniform, although it is slightly enhanced in the Barents Sea (Figure 3-6b), which is consistent with the near-surface air temperature change.

How do these models compare with observed sea ice trends? We calculated the change in sea ice concentration between 1980–1989 and 2005–2014 in the Hadley Centre Sea Ice and Sea Surface Temperature (HadISST) [Rayner et al., 2003] data set. The observations show a reduction in sea ice concentration near the coast from Beaufort Sea to Barents Sea (Figure 3-7). The CESM1 Ensemble and the CMIP5 ensemble also show sea ice loss in the same general region, although the amount lost is much smaller (5-10% versus 10-20%). CMIP5 and CESM1 Large Ensemble also exhibit sea ice loss off the east coast of Greenland, which is not seen in observations.

How does the change in sea ice relate to Arctic amplification? We have already discussed the relationship in terms of the ensemble mean trend. We further address this question by examining the inter-ensemble correlations between the sea ice area and AA. We averaged the sea ice area between 2001–2020 and 2081–2100, and calculated the difference between these two values. There is a strong correlation between the loss of sea ice area and the Arctic amplification in the ensemble members ($\rho = -0.89$, p-value < 0.01, Figure 3-8). The ensemble members with the largest loss of sea ice are also the models with the largest amplification. There is a clear relationship in the CESM1 Large Ensemble between the Arctic amplification and sea ice loss. However, remote processes could also be influencing the Arctic amplification. Do the atmosphere or ocean heat transports have a relation to the Arctic amplification? Are the atmosphere or ocean heat transports somehow related to the changes in sea ice? We explore this further in the next two chapters.

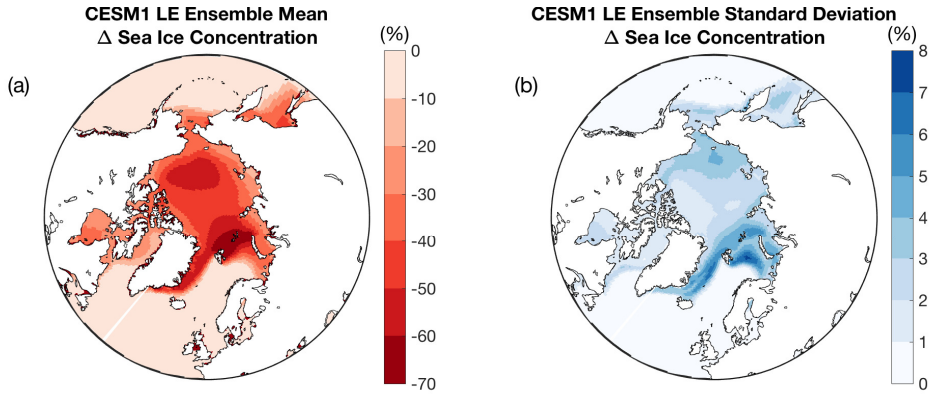

Figure 3-5: Ensemble mean (a) and standard deviation (b) for change in sea ice concentration between 2001–2020 and 2081–2100 for the CESM1 Large Ensemble.

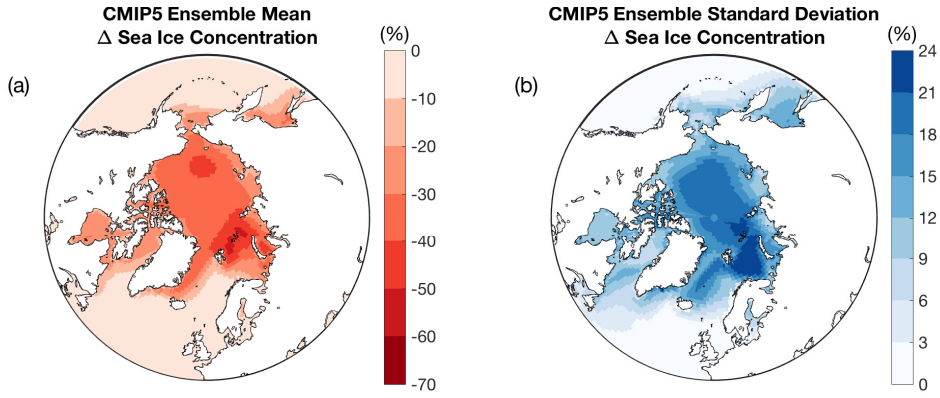

Figure 3-6: Ensemble mean (a) and standard deviation (b) for change in sea ice concentration between 2001–2020 and 2081–2100 for CMIP5.

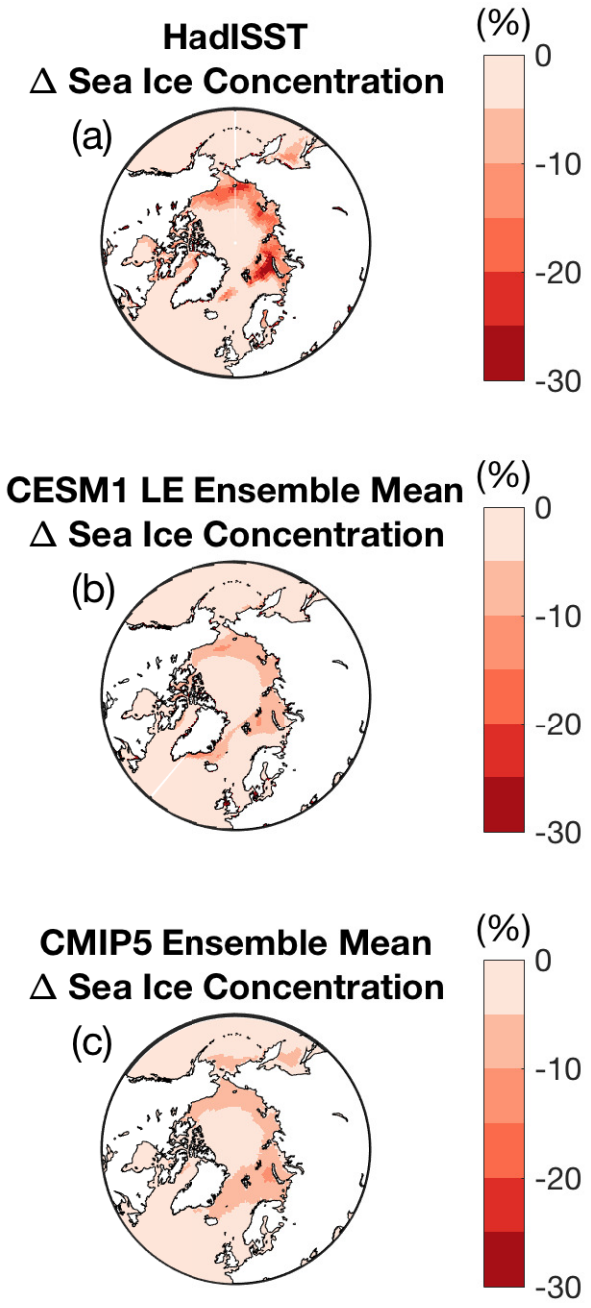

Figure 3-7: Change in sea ice concentration between 1980–1989 and 2005–2014 for (a) HadISST, (b) CESM1 Large Ensemble ensemble mean, and (c) CMIP5 ensemble mean.

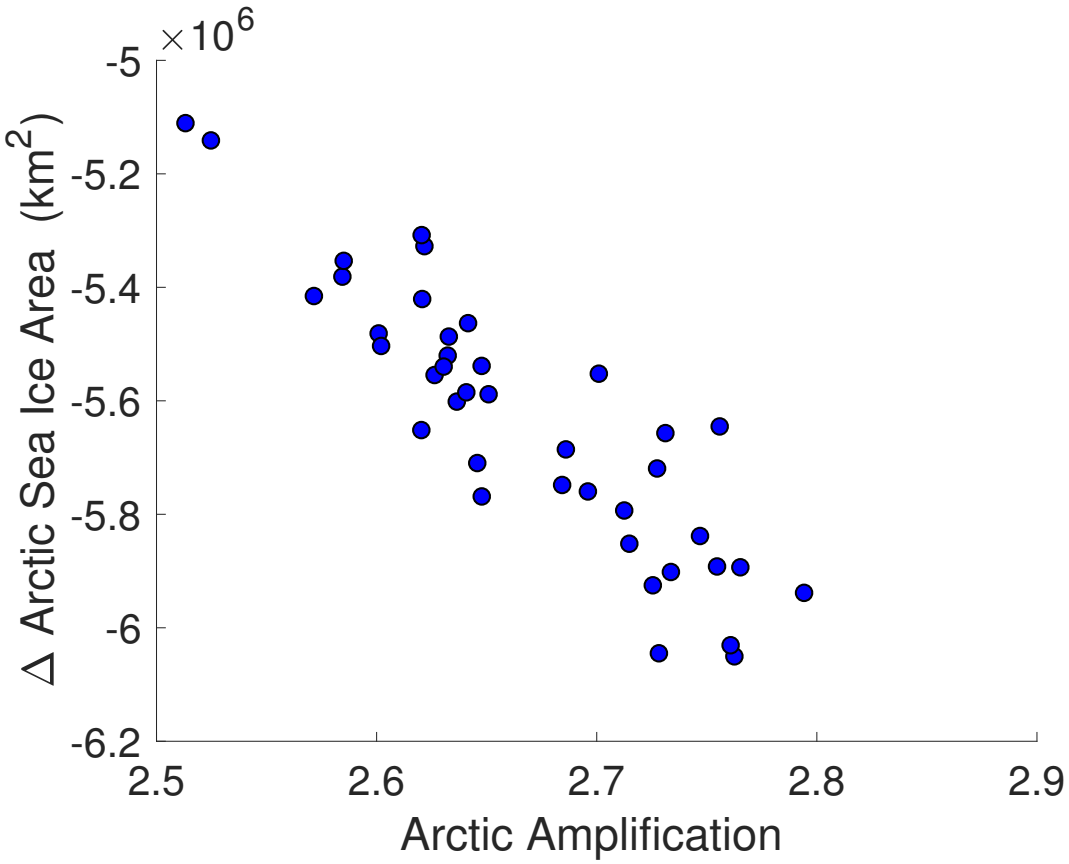

Figure 3-8: Scatterplots of the Arctic amplification vs. the changes in Arctic sea ice area. The correlation is significant to $p < 0.01$.

Chapter 4

Atmosphere Heat Transport

The vertically integrated atmospheric meridional energy flux (AHT) is commonly calculated by integrating the divergence of the zonally averaged surface and top of atmosphere (TOA) fluxes [Peixoto and Oort, 1992, Trenberth and Caron, 2001, Hwang and Frierson, 2010]:

$$[\boldsymbol{F}_A(\phi,t)] = \int_{-\pi/2}^{\phi}\int_{0}^{2\pi} \left\{\boldsymbol{F}^{TOA}(\phi,\lambda,t) - \boldsymbol{F}^{SFC}(\phi,\lambda,t)\right\} a^2\cos\phi\,\mathrm{d}\lambda\,\mathrm{d}\phi \tag{4.1}$$

where a is the radius of the Earth, ϕ is the latitude, and λ is the longitude. Here, [ ] represents zonal averaging. This equation assumes that the total atmospheric energy tendency is negligible. This is a reasonable assumption given the small heat capacity of atmosphere, especially for the monthly or longer time scales. However, if there is an imbalance between the incoming and outgoing solar radiation, it will accumulate at the North Pole. This results in a non-zero northward heat transport at 90°N, which is physically meaningless. For example, the Earth Radiation Budget Experiment (ERBE) satellite measurements have an imbalance of about 6 W/m^2 for the period 1987–1989, which leads to a total heat transport of 3 PW at the North Pole [Wunsch, 2005]. Wunsch [2005] adjusted this error by first assuming a prior value for the total heat transport, $F(\phi)$, and comparing this to the results of the transport from the ERBE, $\tilde{F}(\phi)$. They then used a Bayesian model to adjust each latitude band and nudge the ERBE estimate toward the idealized prior. Trenberth and Caron [2001] found that the ERBE data for the subperiod February 1985 to April 1989 had an imbalance of only a few tenths of watts per meter squared, and did not adjust the ERBE budget. Fasullo and Trenberth [2008] adjusted data from the Clouds and the Earth's Radiant Energy System (CERES) measurements by increasing the outgoing longwave radiation by 1.5 W/m^2

uniformly, and adjusting the albedo rather than the absorbed solar radiation to bring the overall TOA imbalance to an acceptable level of 0.5 PW. There is not an agreed upon "best practice" for adjusting the budget.

The exact, but computationally more expensive, method to calculate AHT uses the velocity, moist static energy (MSE), and kinetic energy [Fasullo and Trenberth, 2008, Farneti and Vallis, 2013]:

$$[\boldsymbol{F}_A(\phi, t)] = \frac{1}{g} \int_0^{2\pi} \mathrm{d}\lambda \int_0^{p_s} a\boldsymbol{v}(p, \phi, \lambda, t) h(p, \phi, \lambda, t) \cos\phi \, \mathrm{d}p, \tag{4.2}$$

where

$$h(p, \phi, \lambda, t) = c_p T + \Phi + Lq + k. \tag{4.3}$$

The fields $\boldsymbol{v}$, T, Φ, q, and k represent wind, temperature, geopotential height, specific humidity, and kinetic energy, respectively. The kinetic energy term is small [Vallis and Farneti, 2009], and we ignore it for the rest of this analysis. The constants $g = 9.8$ m/s^2, $c_p = 1004.64$ J/(kg K), $L = 2.501 \times 10^6$ J/kg, and $a = 6371$ km, correspond to the acceleration due to gravity, the specific heat of air at constant pressure, the latent heat of vaporization, and the radius of the earth, respectively.

The direct method, Equation 4.2, has several advantages over the indirect method, Equation 4.1. The first is that it is more accurate in scenarios with varying external forcing. The second is that with the direct method, we can divide the heat transport into components from the dry static energy and latent energy. In the indirect method, we can only calculate the total transport. For these reasons, the direct method is preferable for this study.

Unfortunately, there are two problems with using this direct method with the CESM1 Large Ensemble. The first problem is that the CESM1 Large Ensemble does not provide output for the geopotential flux term, $\overline{vz}$. This flux term is necessary to calculate the flux of dry static energy (DSE):

$$\overline{vDSE} = c_p \overline{vT} + g\overline{vz} \tag{4.4}$$

Instead, we approximate the DSE using potential temperature [Yang et al., 2015]:

$$DSE = c_p T + gz \approx c_p \theta. \tag{4.5}$$

We calculate the potential temperature as

$$\theta = T\left(\frac{p_0}{p}\right)^{\kappa}, \tag{4.6}$$

where p_0 is the surface pressure, p is the pressure, and $\kappa = 2/7$. Then, the approximate flux due to DSE is:

$$\overline{vDSE} \approx c_p\overline{v\theta} \approx c_p\overline{vT}\left(\frac{\overline{p_0}}{\overline{p}}\right)^{\kappa}. \tag{4.7}$$

The second problem is that the CESM1 Large Ensemble does not store 6-hourly or daily output of the needed 3-dimensional variables (velocity, temperature, humidity, etc.) for all levels of the atmosphere. There are only monthly outputs for these variables and the monthly mean temperature and moisture fluxes ($\overline{vT}$ and $\overline{vq}$). However, the monthly mean velocity has a spurious mass transport, which can be calculated as [Yang et al., 2015]:

$$\overline{v^+} = \frac{\int_0^{2\pi} \mathrm{d}\lambda \int_{p_t}^{p_s} a\overline{v}\cos\phi/g \,\mathrm{d}p}{\int_0^{2\pi} \mathrm{d}\lambda \int_{p_t}^{p_s} a\cos\phi/g \,\mathrm{d}p}, \tag{4.8}$$

where v is the original velocity field, v^+ is the zonally and vertically averaged spurious velocity field, and $\overline{(\quad)}$ represents monthly averaging. Then, the corrected velocity is defined as

$$\overline{v^*} = \overline{v} - \overline{v^+}. \tag{4.9}$$

We also need to correct the monthly mean meridional heat transport, $\overline{vT}$, and the monthly mean meridional moisture transport, $\overline{vq}$:

$$\overline{vq^*} = \overline{vq} - v^+ \int_0^{2\pi} \mathrm{d}\lambda \int_{p_t}^{p_s} qa\cos\phi/g \,\mathrm{d}p \tag{4.10}$$

$$\overline{vT^*} = \overline{vT} - v^+ \int_0^{2\pi} \mathrm{d}\lambda \int_{p_t}^{p_s} Ta\cos\phi/g \,\mathrm{d}p \tag{4.11}$$

Note that vT and vq are calculated at each model time step during the model integration and the monthly mean $\overline{vT}$ and $\overline{vq}$ are saved as output variables by CESM1 Large Ensemble. By applying Equation 4.6, we can calculate the monthly mean meridional dry static energy transport

$$\overline{v\theta^*} = \overline{vT^*}\left(\frac{\overline{p_0}}{\overline{p}}\right)^{\kappa} \tag{4.12}$$

The total atmosphere heat transport by the moist static energy is given by

$$\overline{AHT}_{MSE}^{total} = \int_0^{2\pi} \mathrm{d}\lambda \int_{p_t}^{p_s} \left(c_p \overline{v\theta^*} + L\overline{vq^*}\right) a\cos\phi/g \,\mathrm{d}p. \tag{4.13}$$

This can be decomposed into the contributions from dry static energy,

$$\overline{AHT}_{DSE}^{total} = \int_0^{2\pi} \mathrm{d}\lambda \int_{p_t}^{p_s} c_p \overline{v\theta^*} a\cos\phi/g \,\mathrm{d}p \tag{4.14}$$

and the latent energy,

$$\overline{AHT}_{LE}^{total} = \int_0^{2\pi} \mathrm{d}\lambda \int_{p_t}^{p_s} L\overline{vq^*} a\cos\phi/g \,\mathrm{d}p \tag{4.15}$$

This can be further decomposed into the mean and submonthly transient eddy components:

$$\overline{AHT}_{DSE}^{mean} = \int_0^{2\pi} \mathrm{d}\lambda \int_{p_t}^{p_s} c_p \overline{\theta} \cdot \overline{v^*} a\cos\phi/g \,\mathrm{d}p \tag{4.16}$$

$$\overline{AHT}_{LE}^{mean} = \int_0^{2\pi} \mathrm{d}\lambda \int_{p_t}^{p_s} L\overline{q} \cdot \overline{v^*} a\cos\phi/g \,\mathrm{d}p \tag{4.17}$$

$$\overline{AHT}_{DSE}^{eddy} = \overline{AHT}_{DSE}^{total} - \overline{AHT}_{DSE}^{mean} \tag{4.18}$$

$$\overline{AHT}_{LE}^{eddy} = \overline{AHT}_{LE}^{total} - \overline{AHT}_{LE}^{mean} \tag{4.19}$$

We verified the accuracy of this method using output from a CESM1 historical model run from 2000–2009. We had daily output for this simulation at all levels in the atmosphere. We use the daily output to calculate AHT in two ways: through the accurate equation for moist static energy by explicitly calculating the geopotential flux term:

$$AHT_{MSE}^{daily} = \int_0^{2\pi} \mathrm{d}\lambda \int_{p_t}^{p_s} v\left(c_p T + \Phi + Lq\right) a\cos\phi/g \,\mathrm{d}p, \tag{4.20}$$

and through the approximation for moist static energy using the potential temperature:

$$AHT_{\theta\ approx.}^{daily} = \int_0^{2\pi} \mathrm{d}\lambda \int_{p_t}^{p_s} v\left(c_p \theta + Lq\right) a\cos\phi/g \,\mathrm{d}p. \tag{4.21}$$

We also use monthly output, calculated from this daily output, to calculate the AHT using the potential temperature approximation, as given in Equation 4.13.

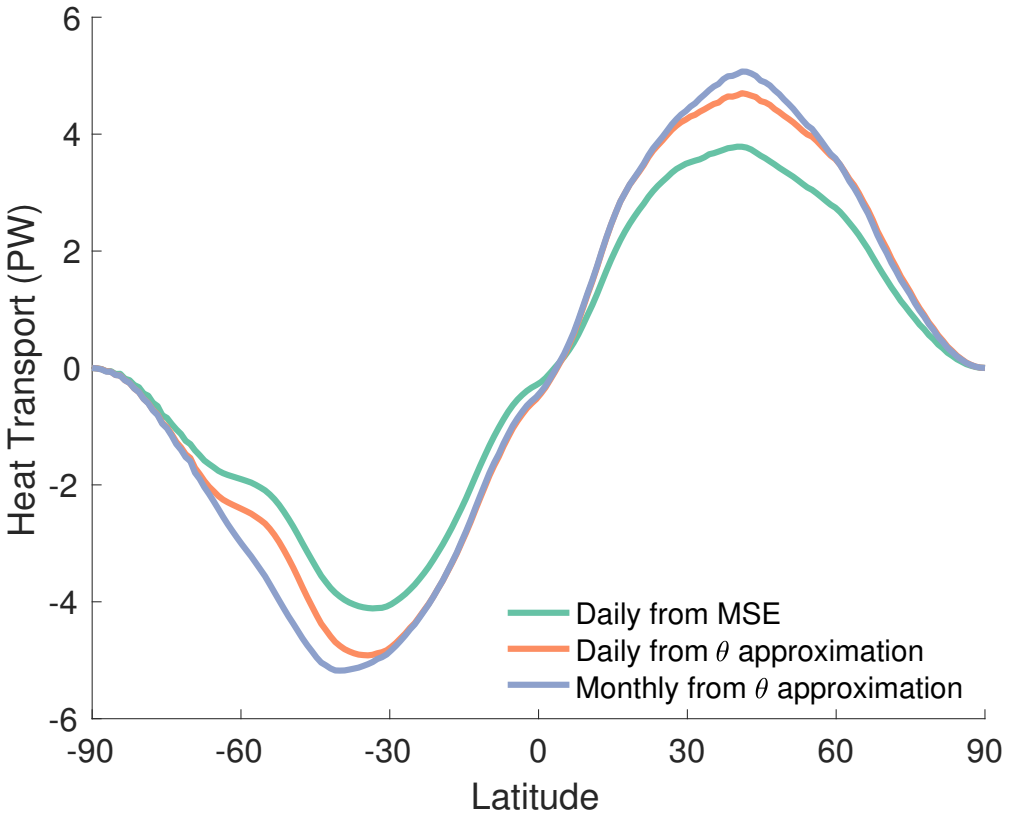

Figure 4-1: The mean atmosphere heat transport calculated from the MSE daily method (green, Eq. 4.20), the daily potential temperature approximation (orange, Eq. 4.21), and the monthly potential temperature approximation (purple, Eq. 4.13) for a CESM1 historical simulation from 2000–2009.

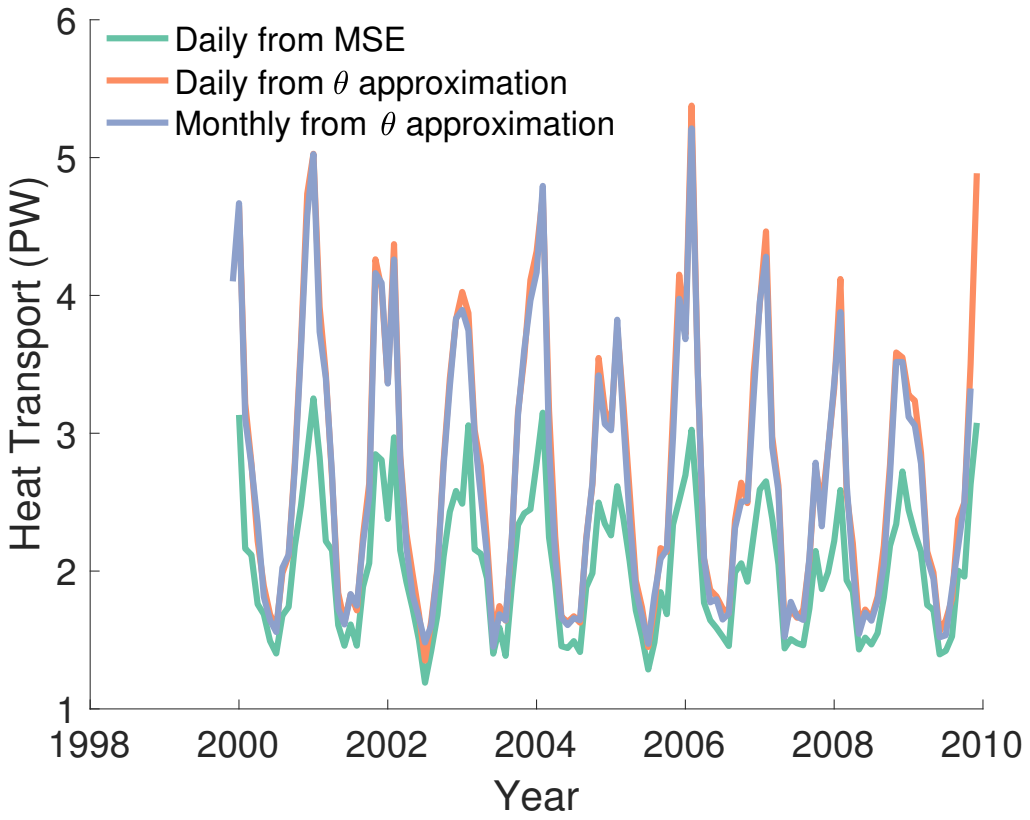

Figure 4-2: The atmosphere heat transport calculated from the MSE daily method (green, Eq. 4.20), the daily potential temperature approximation (orange, Eq. 4.21), and the monthly potential temperature approximation (purple, Eq. 4.13) for a CESM1 historical simulation.

The 10-year mean AHT from daily potential temperature (Figure 4-1, orange) tends to have a larger amplitude than the AHT from daily MSE (Figure 4-1, green). The AHT from monthly potential temperature (Figure 4-1, purple) are very similar to the results from the daily potential temperature, although the amplitude is higher for the monthly values in the midlatitudes. However, near 66°N, the two approximations are nearly identical (Figure 4-2), with a mean value of 2.70 ± 0.97 PW and 2.64 ± 0.94 PW for the daily and monthly approximations of AHT, respectively. The mean of the AHT from daily MSE at 66°N is lower, at 2.03 ± 0.50 PW. Although the approximation using potential temperature slightly overestimates the AHT entering the Arctic, it is the most accurate method available for the CESM1 Large Ensemble with only the monthly mean outputs available.

In the CESM1 Large Ensemble, the total AHT into the Arctic, as defined by the heat transport at 66.5°N, decreases by 0.05 ± 0.03 PW during 1950–2100 (Figure 4-3). This

corresponds to an ensemble mean trend of -3.1×10^{-4} PW/year. To determine if this trend is significant, we used the one-sample Student's t-test for the trends from the 40 ensemble members. The t-test determines if the mean is statistically different from zero. In this case, the trend is significantly different from zero at 5% significance level. The individual components of the AHT also change over this time period. The AHT from the latent energy increases from 0.379 ± 0.004 PW to 0.477 ± 0.006 PW during 1950 – 2100, or 7.4×10^{-4} PW/year (significant at 5%), while the transport from dry static energy decreases from 1.997 ± 0.006 PW to 1.852 ± 0.028 PW during 1950–2100, or -10.4×10^{-4} PW/year (significant at 5%). This is generally consistent with results from Hwang and Frierson [2010] and Hwang et al. [2011] using the CMIP3 multi-model ensemble. As the planet warms, the amount of water vapor the atmosphere can hold increases (e.g. Held and Soden [2006]). More water vapor leads to an increase in latent energy transport, which warms up the Arctic. Furthermore, the Arctic warms up faster than the lower latitude due to various processes and feedback as discussed in the Introduction. This decreases the equator-to-pole temperature gradient, which in turn reduces the poleward heat transport by dry static energy.

The atmosphere heat transport can be divided into monthly mean and submonthly transient eddy terms for the dry static energy and latent energy components (Figure 4-4). The overall decrease in the DSE heat transport is mostly due to the decrease in the eddy term (-8.2×10^{-4} PW/year, significant at 5%). The mean DSE heat transport has a much smaller decrease (-2.2×10^{-4} PW/year, significant at 5%). For the latent energy, most of the increase is due to the eddy term (5.1×10^{-4} PW/year, significant at 5%), although there is also an increase in the mean term (2.2×10^{-4} PW/year, significant at 5%).

How does atmosphere heat transport relate to Arctic amplification? We have already discussed the relationship in terms of the ensemble mean trend. We further address this question by examining the inter-ensemble correlations between the AHT (and its components) and AA. We averaged the heat transport between 2001–2020 and 2081–2100, and calculated the difference between these two values. We computed this value for the total AHT, the DSE and LE components, and the mean and eddy DSE and LE components (Figure 4-5). None of these combinations had a significant ($p < 0.01$) correlation to the Arctic amplification. The ensemble members with a larger increase in AHT are not the models with the largest amplification. Therefore, the strength of AHT into the Arctic does not significantly influence the amplitude of Arctic amplification.

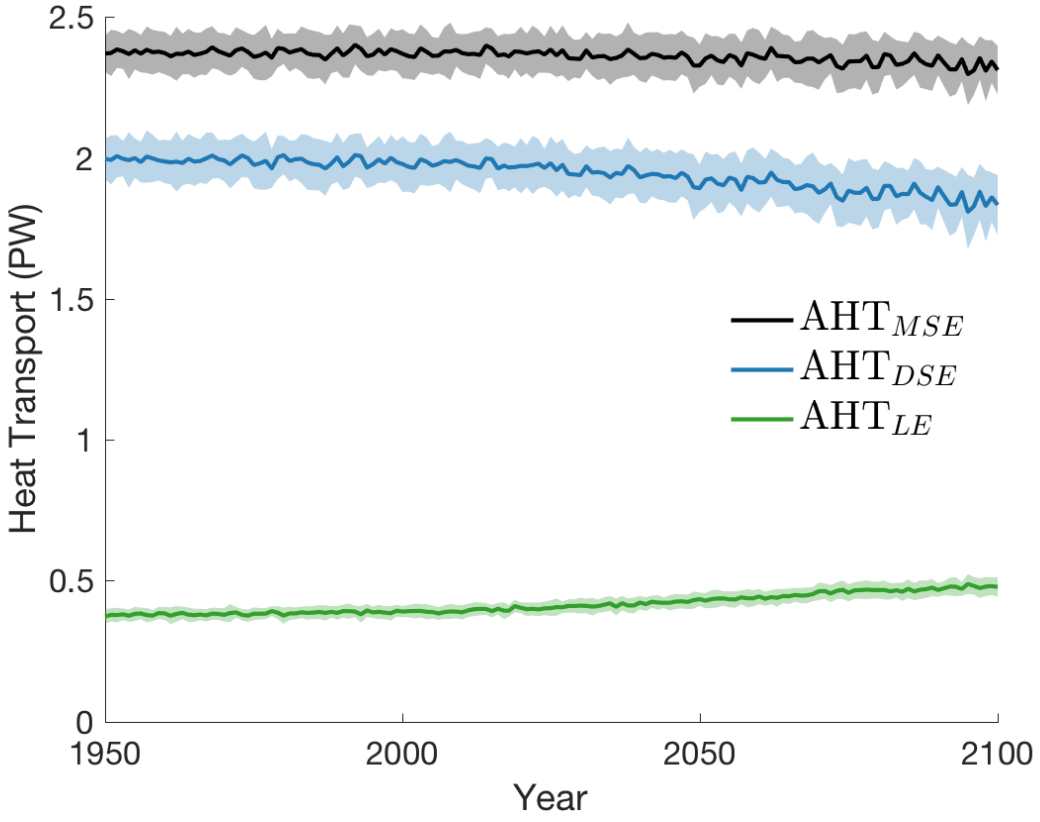

Figure 4-3: The northward atmosphere heat transport at 66.5°N in the CESM1 Large Ensemble. The solid line represents the ensemble mean and the shading represents the standard deviation of the ensemble. This shows the total atmosphere heat transport (black, Eq. 4.13), as well as its components, the transport by dry static energy (blue, Eq. 4.14) and latent energy (green, Eq. 4.15).

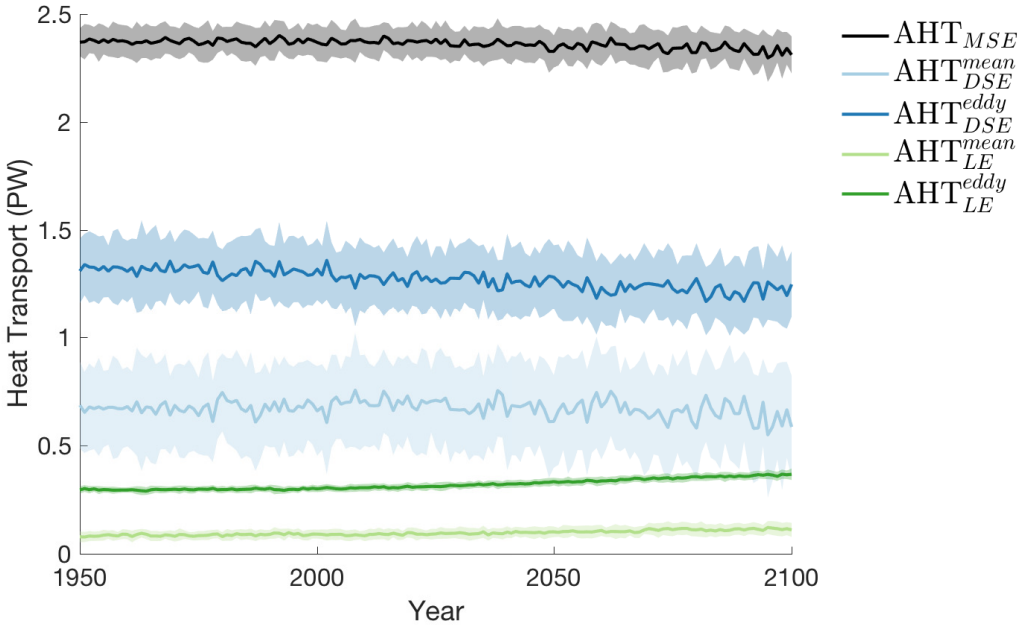

Figure 4-4: The atmosphere heat transport at 66.5°N in the CESM1 Large Ensemble. The solid line represents the ensemble mean and the shading represents the standard deviation of the ensemble. This shows the total atmosphere heat transport (black, Eq. 4.13), as well as its components, the transport by mean dry static energy (light blue, Eq. 4.16), eddy dry static energy (dark blue, Eq. 4.18), mean latent energy (light green, Eq. 4.17), eddy latent energy (dark green, Eq. 4.19).

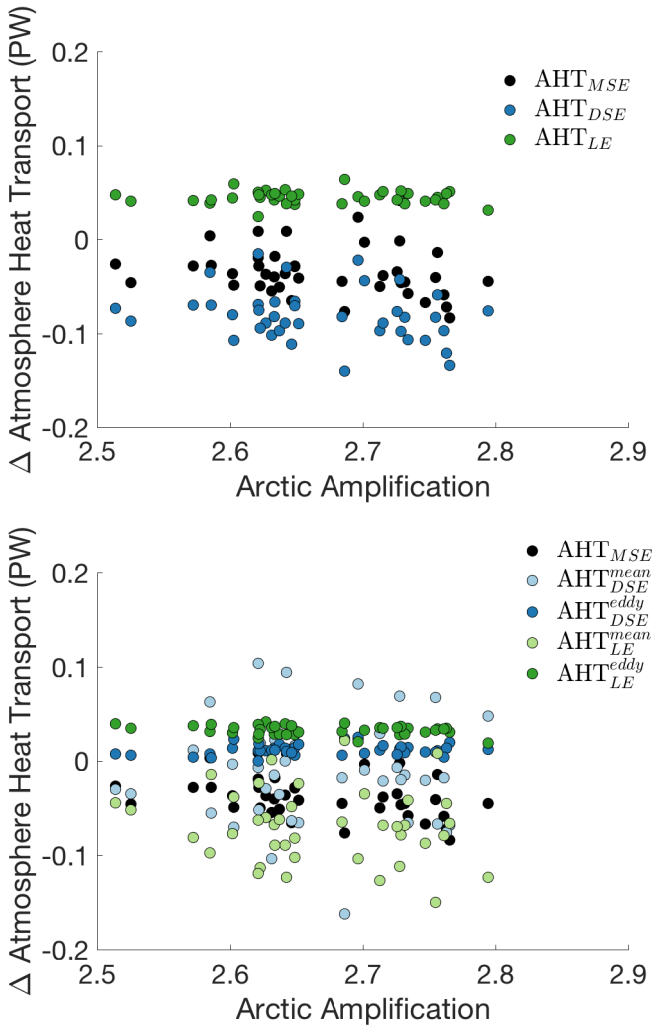

Figure 4-5: Scatterplots of the Arctic amplification vs. the changes in various components of AHT. None of the correlations are significant to $p < 0.01$.

Chapter 5

Ocean Heat Transport

The CESM1 Large Ensemble includes model output for the monthly mean zonally averaged direct ocean heat transport. Previous studies that have studied the effect of ocean heat transport on Arctic amplification have often used this output as the ocean heat transport. These studies typically define the heat moving into the Arctic as the direct zonal mean OHT from the model at 60°N (e.g. Mahlstein and Knutti [2011]), 66–67°N (e.g. Screen et al. [2012], Sun et al. [2015]), or 70°N (e.g. Koenigk and Brodeau [2014], Kay et al. [2012]). This is a somewhat arbitrary decision because it ignores the physical pathways of water into the Arctic. For example, many pick 65°N because it is the latitude of the Bering Strait. In the Atlantic, this latitude circle includes heat transport through the Nordic Sea that may recirculate back southward and never enter the Arctic Ocean. The results from the models' direct ocean heat transport heavily depend on which latitude circle is chosen (Figure 5-1). At 65°N, the mean OHT from 1950–2100 is 0.264 ± 0.002 PW, with the OHT decreasing over time (-2.3×10^{-4} PW/year, significant at 5%). Contrastingly, the mean OHT at 70°N is only 0.178 ± 0.002 PW, and the trend is increasing over time (1.3×10^{-4} PW/year, significant at 5%). The initial choice of latitude can have a large effect on the results. Another issue with using the direct ocean heat transport is that the ocean grid is not parallel to latitude circles. The grid is nearly parallel at low latitudes, but becomes significantly distorted at high latitudes, which can introduce numerical errors into the calculation of the zonal mean.

Instead of picking an arbitrary latitude circle, we define ocean heat transport based on these physical pathways into the Arctic Ocean (Figure 5-2). These sections create a closed domain in the Arctic, which allows for volume budget calculations. Besides being more

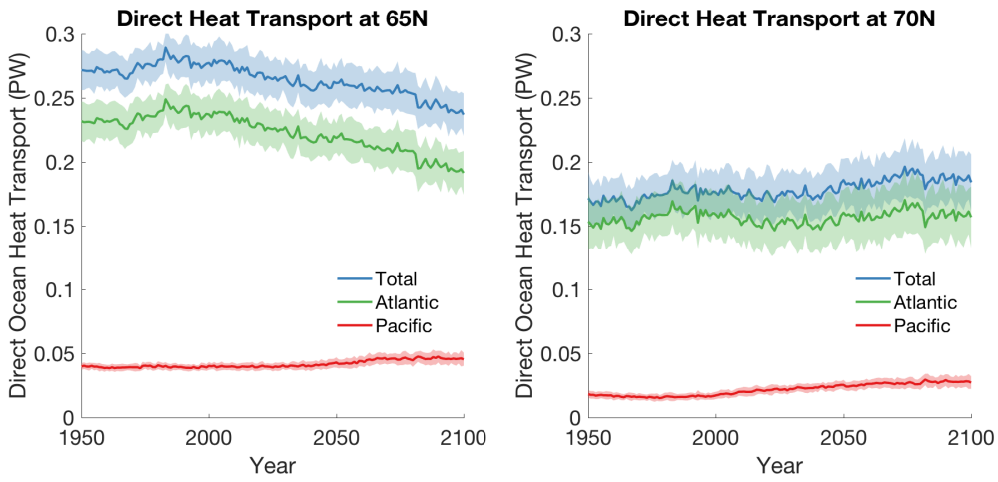

Figure 5-1: The ensemble mean (thick solid line) plus/minus one standard deviation (shading) for the total ocean heat transport (blue), the Atlantic ocean heat transport (green), and the Pacific ocean heat transport (red).

accurate, this method also allows us to look at the changes in ocean heat transport across these five sections individually, instead of only the change in total heat transport. This will help us better understand the relationship between ocean heat transport and Arctic amplification by directly relating each OHT component with the corresponding regional sea ice change. It is also easier to compare to observations.

For each ensemble members, the heat and volume transport are calculated using the Physical Analysis of the Gridded Ocean (PAGO) suite of programs, introduced by Deshayes et al. [2014]. It calculates heat and volume transports using monthly velocity and temperature fields across predefined sections. These monthly transports are then averaged over the year, from January to December.

In the CESM1 Large Ensemble, the ensemble mean of the total volume transport into the Arctic does not change very much between 1950 and 2100 (Figure 5-3). There is a trend of -1.7×10^{-6} Sv/year (not significant at 5%), which corresponds to an overall decrease of -0.0004 ± 0.0020 Sv between 1950–2100. There is a slight decrease in northward volume transport in the Bering Strait (-9.1 $\times 10^{-4}$ Sv/year, significant at 5%) and Nares Strait (-4.6 $\times 10^{-4}$ Sv/year, significant at 5%), but this is largely compensated by a slight increase in northward transport in the Barrow Strait (13.2 $\times 10^{-4}$ Sv/year, significant at 5%). The volume transport across Barents Sea Opening and Fram Strait remain nearly steady, and the trends are not significantly different from zero.

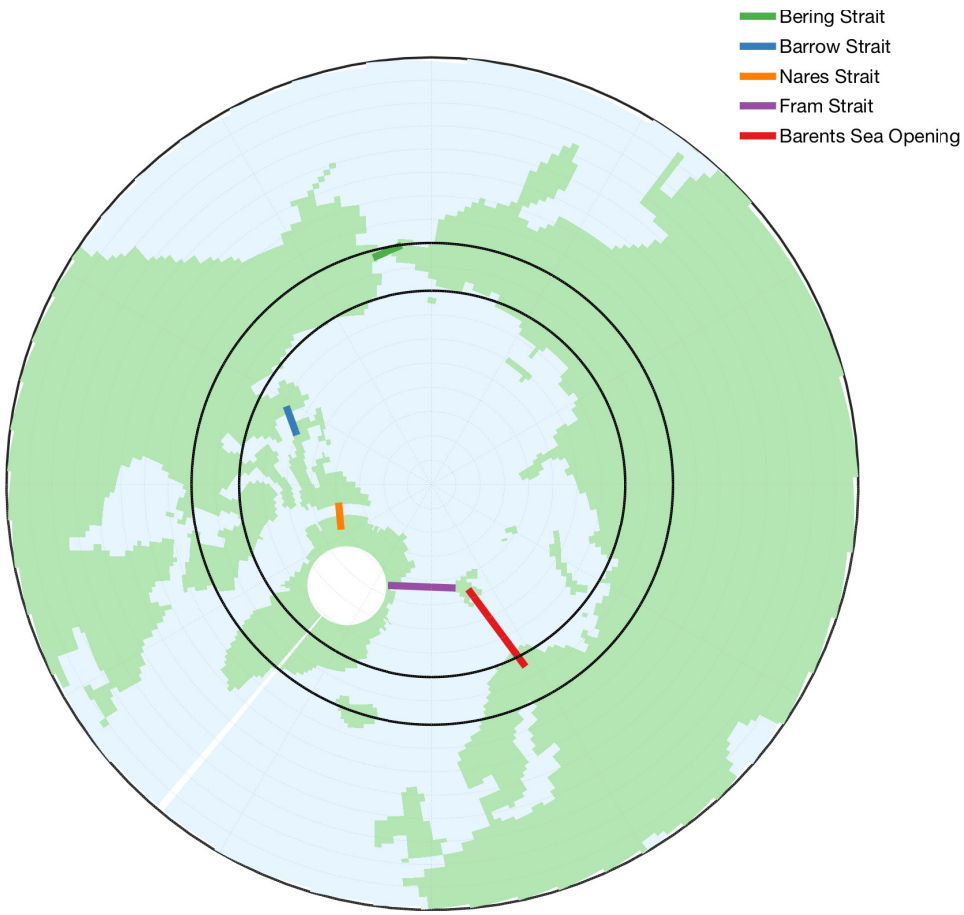

Figure 5-2: Definitions of Arctic sections. They are overlaid on the CESM1 model grid. The 65th parallel north and 70th parallel north are shown in black.

Volume Transport (Sv)	CESM1 Large Ensemble	CCSM4	Observation-Based Inverse Model
Barents Sea	2.37	2.3	2.3 ± 1.2
Barrow Strait	-0.21	-0.3	
Bering Strait	0.87	1.1	0.7 ± 0.7
Fram Strait	-1.68	-1.8	-1.1 ± 1.2
Nares Strait	-1.35	-1.5	
Davis Strait			-2.1 ± 0.7
Net Transport	-1.3×10^{-4}	-0.2	-0.2 ± 0.08

Table 5.1: Climatological Arctic volume fluxes. The CESM1 Large Ensemble values are calculated as the average of the 1950–2100 value of the 40 ensemble members. The CCSM4 values are calculated as average of the 1981–2005 from six CCSM4 ensemble members [Jahn et al., 2012]. The observations are the annual average transports between September 2005–August 2006 [Tsubouchi et al., 2018]. All units are in Sv.

The volume transports in the CESM1 Large Ensemble generally agree with an ensemble from CCSM4 [Jahn et al., 2012] (Table 5.1). The largest discrepancy is in the Bering Strait, where the CESM1 Large Ensemble has 0.866 ± 0.008 Sv transport, but the CCSM4 has a transport of 1.1 Sv. CESM1 Large Ensemble overestimates the strength of the volume transport in Barents Sea Opening, Bering Strait, and Fram Strait, compared to observations from Tsubouchi et al. [2018], although the difference could be due to the fact that the observation is only one year long. CESM1 Large Ensemble underestimates the strength of the southbound transport through the Canadian Arctic Archipelago, with a combined -1.56 ± 0.02 Sv through the Nares and Barrow Straits, compared to -2.1 Sv through Davis Strait in the observations.

Between 1950 and 2100, the ensemble mean heat transport into the Arctic greatly increases (Figure 5-4). The total OHT doubles, increasing from 0.048 ± 0.004 PW from 1950–1959 to 0.095 ± 0.005 PW from 2091 – 2100. Most of this increase is due to the increase across the Barents Sea Opening, which increases from 0.027 ± 0.004 PW to 0.059 ± 0.004 PW in that time. The OHT across Fram Strait is relatively steady between 1950 and 2000 (7.0×10^{-6} PW/year, not significant at 5%), then increases between 2000 and 2075 (2.0×10^{-4} PW/year, significant at 5%), and then decreases until 2100 (-3.1×10^{-4} PW/year, significant at 5%). Overall, this leads to an increase of 0.010 ± 0.004 PW during 1950–2100. The transport across Bering Strait is relatively steady from 1950 through 2000 (3.0×10^{-6} PW/year, not significant at 5%) and then increases until 2100 (1.2×10^{-4} PW/year, significant at 5%). This leads to an overall increase of 0.011 ± 0.001 PW during 1950–2100.

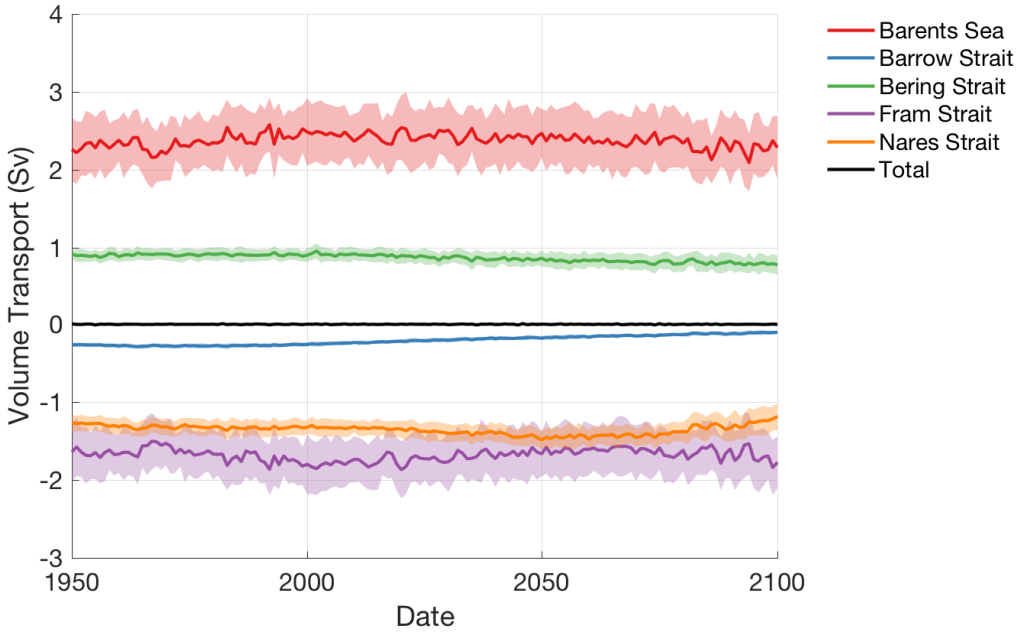

Figure 5-3: Volume transport in the CESM1 Large Ensemble. The thick line represents the ensemble mean and the shading represents one standard deviation.

Nares Strait decreases slightly during 1950–2050 (-1.4×10^{-6} PW/year, significant at 5%), and then decreases (-8.3×10^{-5} PW/year, significant at 5%). This leads to a decrease by -0.0037 ± 0.0003 PW during 1950–2100. The OHT through Barrow Strait is relatively steady until 2000 (-4.1×10^{-7} PW/year, not significant at 5%) and then decreases until 2100 (-1.5×10^{-5} PW/year, significant at 5%), which lead to a decrease of -0.0016 ± 0.0001 PW during 1950–2100.

If the OHT is related to Arctic amplification, we reason that it is because there is an increase in heat being brought into the Arctic. Therefore we want to compare the Arctic amplification of each ensemble member with the change in OHT during this period. For each ensemble, we calculated the average OHT across each sections for the time periods 2001–2020 and 2081–2100. We then calculated the difference between the values, ΔOHT, for the five Arctic sections and the sum of the five sections. The change in total heat transport is strongly correlated with the Arctic amplification in the ensemble members ($\rho = 0.56, p < 0.01$, Figure 5-5, black). The Barents Sea Opening has the largest increase in OHT, and consequently has the strongest correlation to Arctic amplification ($\rho = 0.50, p < 0.01$, Figure 5-5, red).

Why is the ocean heat transport across the Barents Sea opening related to the Arctic amplification in the CESM1 Large Ensemble? As shown in Chapter 3, there is sea ice loss

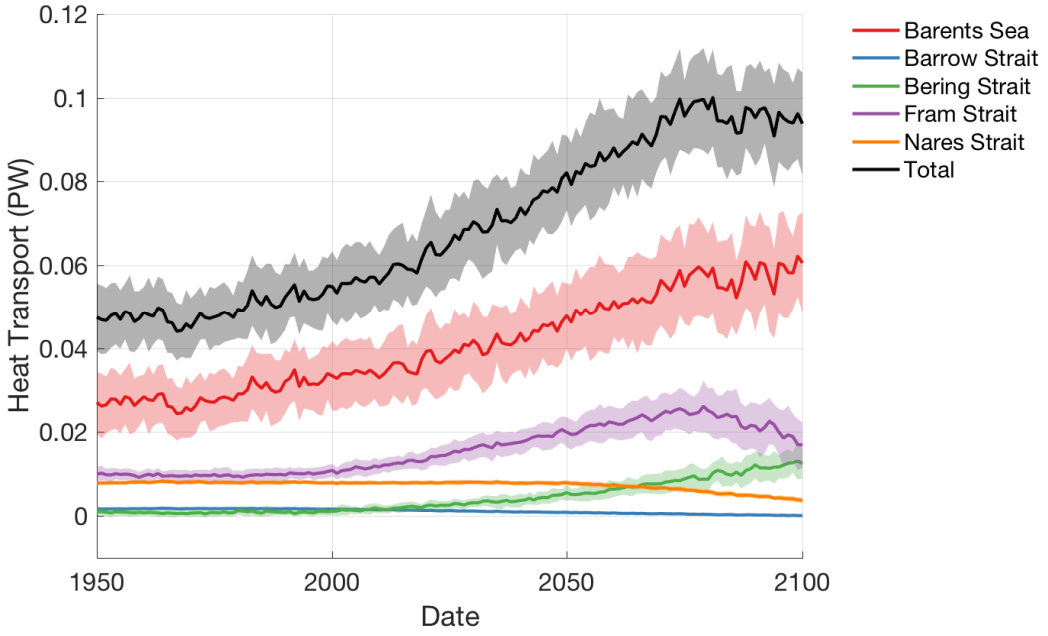

Figure 5-4: Heat transport in the CESM1 Large Ensemble. The thick line represents the ensemble mean and the shading represents one standard deviation.

throughout the Arctic in the CESM1 Large Ensemble. However, it is not spatially uniform. Barents Sea is the region with the highest amount of sea ice loss (Figure 3-5). Barents Sea is also the area with the highest ensemble spread of sea ice loss and the surface air temperature warming.

To investigate this further, we defined a time series for the Barents Sea ice as simply the sum total area of sea ice in the northern hemisphere between 20°E and 110°E (Figure 5-6, blue). This segment has a mean sea ice area of $(2.11 \pm 0.08) \times 10^6$ km^2 from 1950 – 1959, which decreases to $(0.56 \pm 0.06) \times 10^6$ km^2 from 2091– 2100. The amount of OHT across Barents Sea Opening increases from 27.2 ± 3.7 TW to 59.1 ± 4.0 TW during the same time period (Figure 5-6, red). For each ensemble member, we calculated the correlation between the time series for the Barents Sea ice area and the Barents Sea Opening ocean heat transport. All ensemble members showed a very strong correlation, with a correlation coefficient is at least -0.75 for all ensembles, and all p-values are less than 0.01. This suggests that the increase of heat across Barents Sea Opening is melting the sea ice in the Barents Sea. When the sea ice melts, this drastically changes the local albedo. Now, more incoming radiation is being absorbed by the ocean instead of being directed back into space (Figure 5-7a, orange). When sea ice melts, it also exposes the ocean to the atmosphere above it.

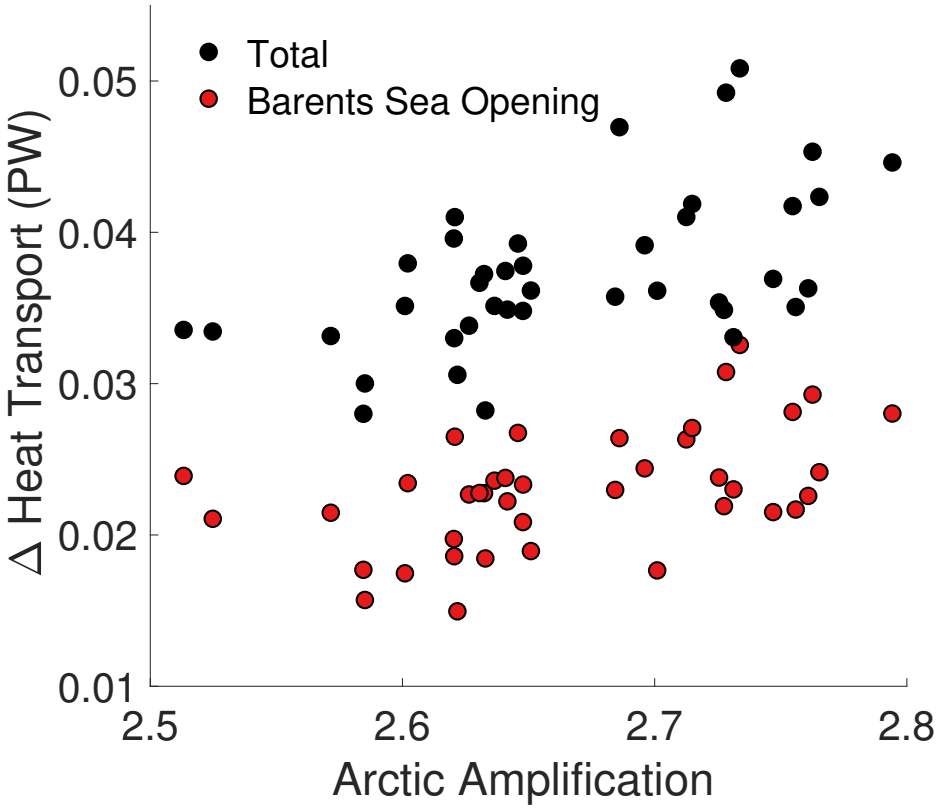

Figure 5-5: Scatterplots of the Arctic amplification vs. the changes in total OHT (black) and Barents Sea Opening OHT (red). Both correlations are significant to $p < 0.01$.

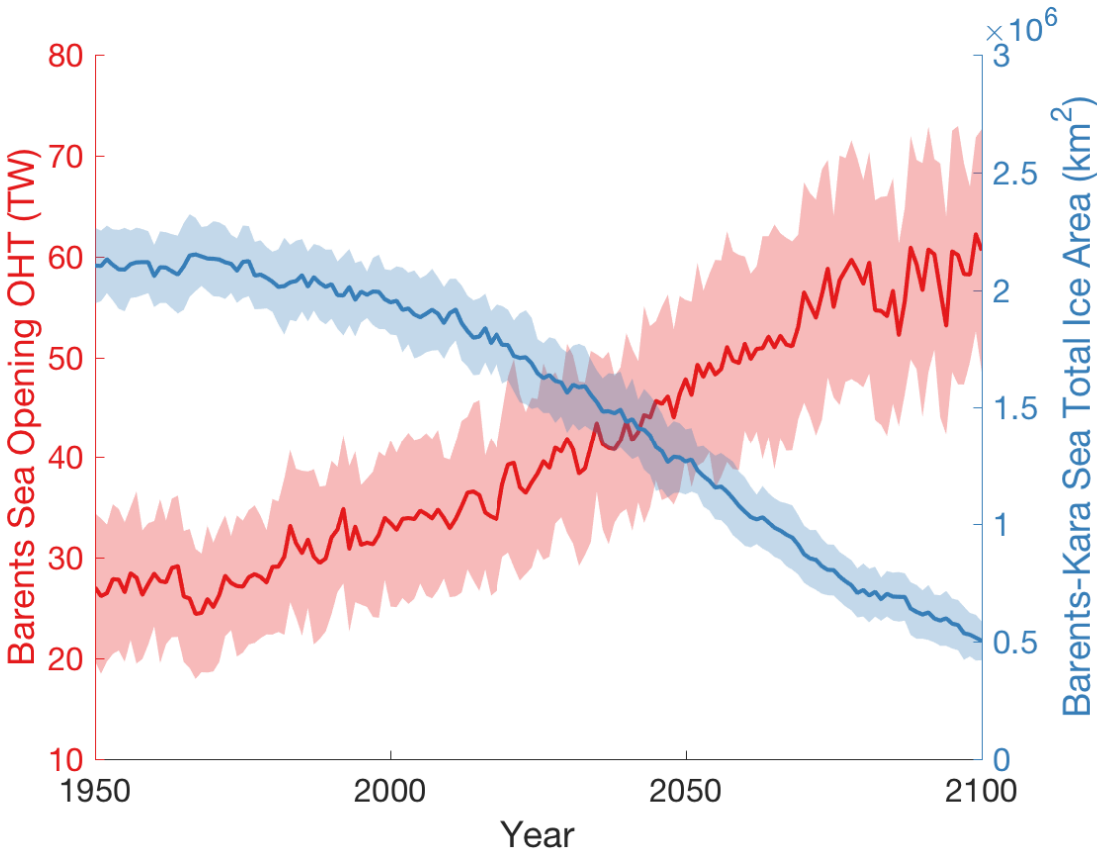

Figure 5-6: Time series of the ocean heat transport across the Barents Sea Opening (red), and time series of the total sea ice area in the Barents-Kara Sea (blue). The thick line represents the ensemble mean and the shading represents one standard deviation.

This allows the ocean to export more heat to the atmosphere (Figure 5-7a, purple), which could also increase surface temperatures. It also increases downward longwave radiation (Figure 5-7b, green), due to cloud feedback.

We calculated the change in sea ice concentration between 2001–2020 and 2081–2100. There was a strong correlation ($\rho = -0.81$, p-value < 0.01) between an increase in OHT across the Barents Sea Opening and a decrease in sea ice in the Barents-Kara Sea. The ensemble members with higher increases in Barents Sea OHT melt more sea ice. Those members then have an increase in absorbed shortwave radiation (Figure 5-8a, orange), turbulent heat flux (Figure 5-8a, purple), and downward longwave heat flux (Figure 5-8b, green) which leads to higher warming in the Arctic.

A similar mechanism is happening near the Bering Strait. We define the Beaufort-Chukchi Sea ice time series as the total area of sea ice in the northern hemisphere between

160°E and 130°W. The CESM1 Large Ensemble ensemble mean sea ice area decreased from $(3.12 \pm 0.07) \times 10^6$ km^2 from 1950 – 1959, to $(1.09 \pm 0.07) \times 10^6$ km^2 2091– 2100 (Figure 5-9, blue), while the OHT through Bering Strait increased from 0.9 ± 0.4 TW to 12.0 ± 1.3 TW in that time span (Figure 5-9, red). For each ensemble member, we calculated the correlation between the time series for the Beaufort-Chukchi Sea Ice Area and the Bering Strait ocean heat transport. All ensemble members showed a very strong correlation, with a correlation coefficient is at least -0.89, and p-values less than 0.01. We also calculated the change in sea ice concentration between 2001–2020 and 2081–2100. There was a strong correlation ($\rho = -0.66$, p-value < 0.01) between an increase in OHT across the Bering Strait and a decrease in sea ice in the Beaufort-Chukchi Sea across the CESM1 Large Ensemble. The CESM1 Large Ensemble members that happened to have a larger increase in ocean heat transport were the models with highest Arctic amplification. We suggest that this is because the ocean heat transport is melting the sea ice margin. This creates a positive feedback loop, where the net surface shortwave heat flux, net turbulent heat flux, and downward surface longwave heat flux are increasing, which increases surface temperatures.

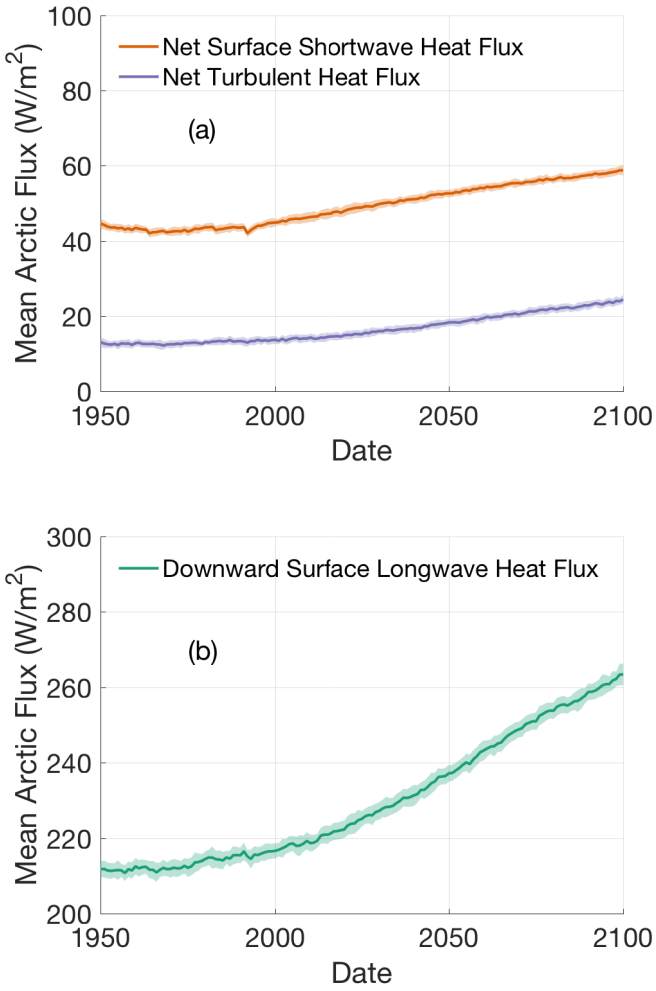

Figure 5-7: Time series of the area-weighted mean (a) net surface shortwave heat flux (orange), and net surface turbulent heat flux (purple), and (b) downward surface longwave heat flux (green), for the area north of 66.5°N. The thick line represents the ensemble mean and the shading represents one standard deviation.

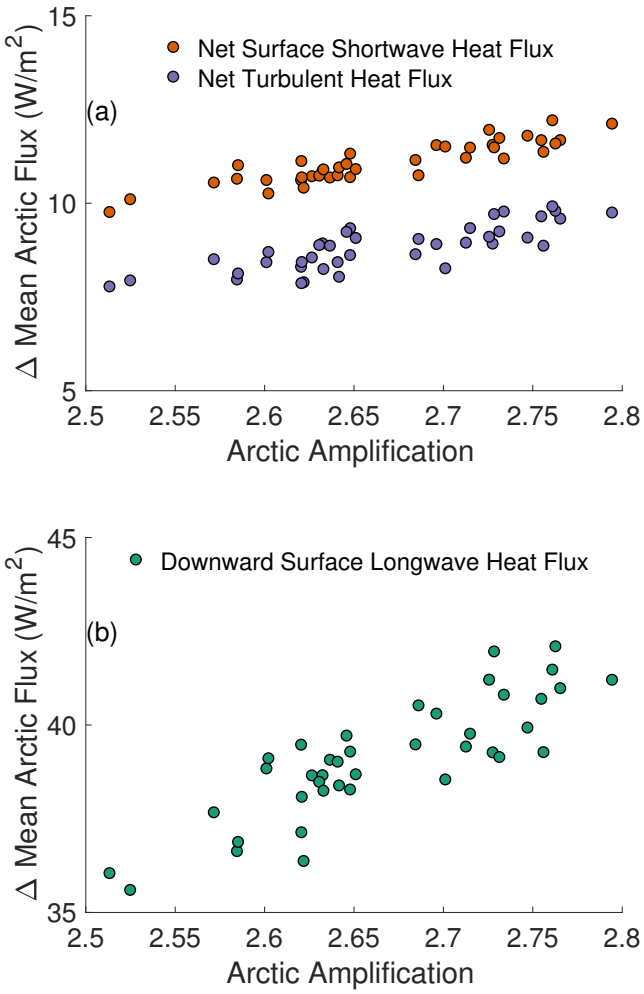

Figure 5-8: Scatterplots of the (a) Arctic amplification vs. net surface shortwave heat flux (orange), and net surface turbulent heat flux (purple), and (b) Arctic amplification vs. the changes in downward surface longwave heat flux (green). All correlations are significant to $p < 0.01$.

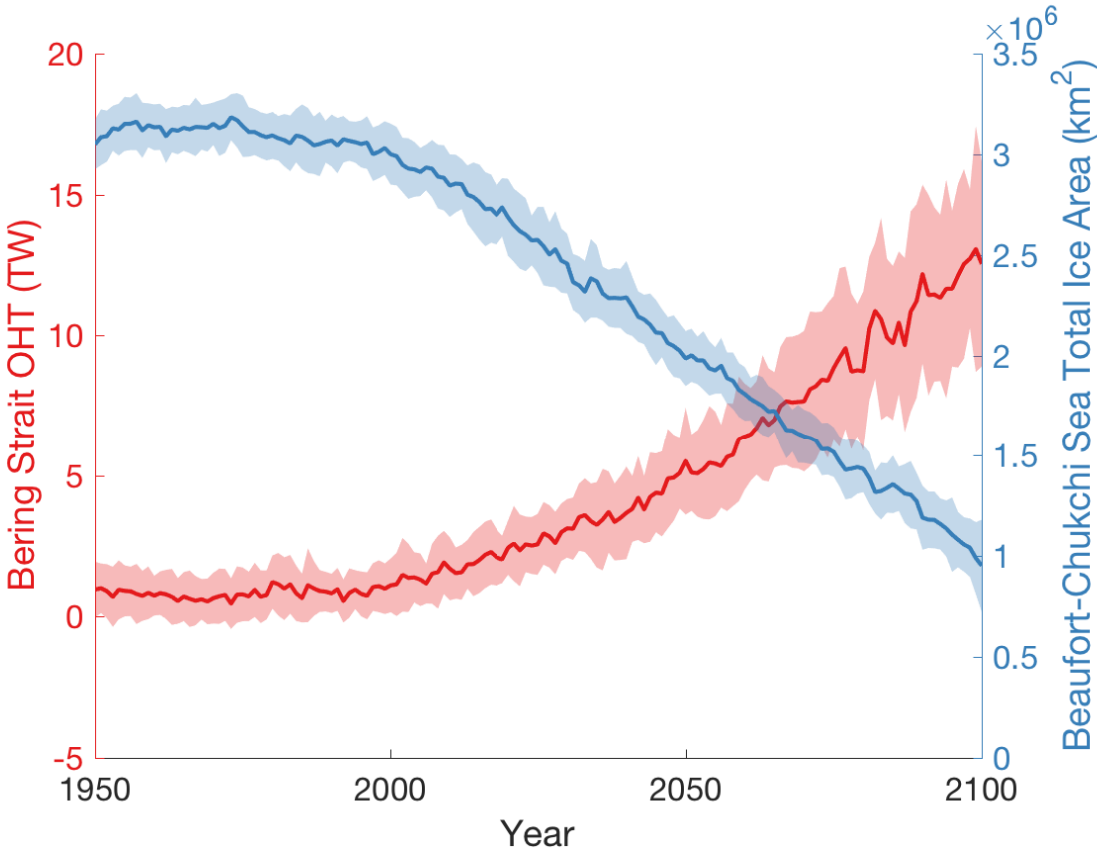

Figure 5-9: Time series of the ocean heat transport across the Bering Strait (red), and time series of the total sea ice area in the Beaufort-Chukchi Sea (blue). The thick line represents the ensemble mean and the shading represents one standard deviation.

Chapter 6

Conclusions

The Arctic air temperature has warmed nearly twice as much as the global mean in the previous decades. This thesis used a novel approach to investigate how ocean heat transport affects Arctic amplification. Instead of using the zonally averaged ocean heat transport near the Arctic circle, we used the ocean heat transport across the various sections that enclose the Arctic Ocean. This takes into account the physical boundaries of the Arctic. Also, instead of only looking at one ensemble member from one model, we looked at 40 ensemble members from one model. This allows us to cleanly isolate the effect of climate change from that of internal variability of the model's climate system without contamination from model-to-model difference, which is a major limitation of the multi-model ensemble. Furthermore, we used the inter-ensemble spread due to the internal variability for better attribution which is often obscured by a strong trend. We found that the ensemble members that happened to have a larger increase in ocean heat transport across the Barents Sea Opening were the models with highest Arctic amplification. We suggest that this is because the ocean heat transport is melting the sea ice margin. This creates a positive feedback loop from several mechanisms. The surface albedo lowers, and therefore the absorbed shortwave radiation increases. More of the Arctic Ocean is exposed to the atmosphere, which increases the amount of turbulent heat flux transferred from the ocean to the atmosphere. Finally, cloud coverage changes, which increased the downward longwave radiation at the surface. Although the ensemble members have changes in the atmosphere heat transport that are on the same order as the ocean heat transport, they do not correlate with Arctic amplification. This suggests that increasing the atmospheric heat transport from the midlatitudes does not

lead to Arctic amplification by itself. Instead, the feedback between the sea ice melt and ocean heat transport is necessary to explain the spread in Arctic amplification.

Bibliography

V. A. Alexeev, P. L. Langen, and J. R. Bates. Polar amplification of surface warming on an aquaplanet in "ghost forcing" experiments without sea ice feedbacks. *Climate Dynamics*, 24(7):655–666, Jun 2005. ISSN 1432-0894. doi: 10.1007/s00382-005-0018-3. URL https://doi.org/10.1007/s00382-005-0018-3.

John Antonov. World Ocean Atlas 1998: Temperature of the Atlantic Ocean, 1998.

Allison H. Baker, Haiying Xu, John M. Dennis, Michael N. Levy, Doug Nychka, Sheri A. Mickelson, Jim Edwards, Mariana Vertenstein, and Al Wegener. A methodology for evaluating the impact of data compression on climate simulation data. In *Proceedings of the 23rd International Symposium on High-performance Parallel and Distributed Computing*, HPDC '14, pages 203–214, New York, NY, USA, 2014. ACM. ISBN 978-1-4503-2749-7. doi: 10.1145/2600212.2600217. URL http://doi.acm.org/10.1145/2600212.2600217.

Judah Cohen. Arctic change and possible influence on mid-latitude climate and weather. 03 2018. doi: 10.5065/D6TH8KGW.

Josefino C. Comiso, Claire L. Parkinson, Robert Gersten, and Larry Stock. Accelerated decline in the Arctic sea ice cover. *Geophysical Research Letters*, 35(1), 2008. doi: 10.1029/2007GL031972. URL https://agupubs.onlinelibrary.wiley.com/doi/abs/10.1029/2007GL031972.

Gilbert P Compo, Jeffrey S Whitaker, Prashant D Sardeshmukh, N Matsui, RJ Allan, X Yin, BE Gleason, RS Vose, G Rutledge, P Bessemoulin, et al. The twentieth century reanalysis project. *Quarterly Journal of the Royal Meteorological Society*, 137(654):1–28, 2011.

D. P. Dee, S. M. Uppala, A. J. Simmons, P. Berrisford, P. Poli, S. Kobayashi, U. Andrae, M. A. Balmaseda, G. Balsamo, P. Bauer, P. Bechtold, A. C. M. Beljaars, L. van de Berg, J. Bidlot, N. Bormann, C. Delsol, R. Dragani, M. Fuentes, A. J. Geer, L. Haimberger, S. B. Healy, H. Hersbach, E. V. Hólm, L. Isaksen, P. Kållberg, M. Köhler, M. Matricardi, A. P. McNally, B. M. Monge-Sanz, J.-J. Morcrette, B.-K. Park, C. Peubey, P. de Rosnay, C. Tavolato, J.-N. Thépaut, and F. Vitart. The ERA-Interim reanalysis: configuration and performance of the data assimilation system. *Quarterly Journal of the Royal Meteorological Society*, 137(656):553–597, 2011. doi: 10.1002/qj.828. URL http://dx.doi.org/10.1002/qj.828.

Clara Deser, Reto Knutti, Susan Solomon, and Adam S. Phillips. Communication of the role of natural variability in future North American climate. *Nature Climate Change*, 2: 775 EP –, 10 2012. URL https://doi.org/10.1038/nclimate1562.

Julie Deshayes, Ruth Curry, and Rym Msadek. CMIP5 model intercomparison of freshwater budget and circulation in the North Atlantic. *Journal of Climate*, 27(9):3298–3317, 2014. doi: 10.1175/JCLI-D-12-00700.1. URL https://doi.org/10.1175/JCLI-D-12-00700.1.

Environmental Working Group (EWG). Joint U.S.–Russian atlas of the Arctic Ocean for the winter period. National Snow and Ice Data Center, 1997.

Riccardo Farneti and Geoffrey K. Vallis. Meridional energy transport in the coupled atmosphere–ocean system: Compensation and partitioning. *Journal of Climate*, 26(18):7151–7166, 2013. doi: 10.1175/JCLI-D-12-00133.1. URL https://doi.org/10.1175/JCLI-D-12-00133.1.

John T. Fasullo and Kevin E. Trenberth. The annual cycle of the energy budget. Part II: Meridional structures and poleward transports. *Journal of Climate*, 21(10):2313–2325, may 2008. doi: 10.1175/2007jcli1936.1.

Nicole Feldl, Bruce T. Anderson, and Simona Bordoni. Atmospheric eddies mediate lapse rate feedback and Arctic amplification. *Journal of Climate*, 30(22):9213–9224, 2017. doi: 10.1175/JCLI-D-16-0706.1. URL https://doi.org/10.1175/JCLI-D-16-0706.1.

Rune G. Graversen and Mattias Burtu. Arctic amplification enhanced by latent energy transport of atmospheric planetary waves. *Quarterly Journal of the Royal Meteorological Society*, 142(698):2046–2054, 2016. doi: 10.1002/qj.2802. URL https://rmets.onlinelibrary.wiley.com/doi/abs/10.1002/qj.2802.

Rune G. Graversen, Thorsten Mauritsen, Michael Tjernström, Erland Källén, and Gunilla Svensson. Vertical structure of recent Arctic warming. *Nature*, 451:53 EP –, 01 2008. URL https://doi.org/10.1038/nature06502.

Rune G. Graversen, Thorsten Mauritsen, Sybren Drijfhout, Michael Tjernström, and Sebastian Mårtensson. Warm winds from the Pacific caused extensive Arctic sea-ice melt in summer 2007. *Climate Dynamics*, 36(11):2103–2112, Jun 2011. ISSN 1432-0894. doi: 10.1007/s00382-010-0809-z. URL https://doi.org/10.1007/s00382-010-0809-z.

Alex Hall. The role of surface albedo feedback in climate. *Journal of Climate*, 17(7): 1550–1568, 2004. doi: 10.1175/1520-0442(2004)017<1550:TROSAF>2.0.CO;2. URL https://doi.org/10.1175/1520-0442(2004)017<1550:TROSAF>2.0.CO;2.

Ed Hawkins and Rowan Sutton. The potential to narrow uncertainty in regional climate predictions. *Bulletin of the American Meteorological Society*, 90(8):1095–1108, 2009. doi: 10.1175/2009BAMS2607.1. URL https://doi.org/10.1175/2009BAMS2607.1.

I. M. Held and B .J. Soden. Robust responses of the hydrological cycle to global warming. *J. Climate*, 19(21):5686–5699, 2006.

Yen-Ting Hwang and Dargan M. W. Frierson. Increasing atmospheric poleward energy transport with global warming. *Geophysical Research Letters*, 37(24), 2010. ISSN 1944-8007. doi: 10.1029/2010GL045440. URL http://dx.doi.org/10.1029/2010GL045440. L24807.

Yen-Ting Hwang, Dargan M. W. Frierson, and Jennifer E. Kay. Coupling between Arctic feedbacks and changes in poleward energy transport. *Geophysical Research Letters*, 38(17), 2011. ISSN 1944-8007. doi: 10.1029/2011GL048546. URL http://dx.doi.org/10.1029/2011GL048546. L17704.

Alexandra Jahn, Kara Sterling, Marika M. Holland, Jennifer E. Kay, James A. Maslanik, Cecilia M. Bitz, David A. Bailey, Julienne Stroeve, Elizabeth C. Hunke, William H. Lipscomb, and Daniel A. Pollak. Late-twentieth-century simulation of Arctic sea ice and ocean properties in the CCSM4. *Journal of Climate*, 25(5):1431–1452, 2012. doi: 10.1175/JCLI-D-11-00201.1. URL https://doi.org/10.1175/JCLI-D-11-00201.1.

E. Kalnay, M. Kanamitsu, R. Kistler, W. Collins, D. Deaven, L. Gandin, M. Iredell, S. Saha, G. White, J. Woollen, Y. Zhu, M. Chelliah, W. Ebisuzaki, W. Higgins, J. Janowiak, K. C. Mo, C. Ropelewski, J. Wang, A. Leetmaa, R. Reynolds, Roy Jenne, and Dennis Joseph. The NCEP/NCAR 40-year reanalysis project. *Bulletin of the American Meteorological Society*, 77(3):437–472, 1996. doi: 10.1175/1520-0477(1996)077<0437:TNYRP>2.0.CO;2. URL https://doi.org/10.1175/1520-0477(1996)077<0437:TNYRP>2.0.CO;2.

M. Kanamitsu, W. Ebisuzaki, J. Woollen, S.K. Yang, JJ Hnilo, M. Fiorino, and GL Potter. NCEP-DOE AMIP-II reanalysis (R-2). *Bull. Amer. Meteor. Soc*, 83(11):1631–1643, 2002.

Marie Kapsch, R Graversen, and Michael Tjernström. Springtime atmospheric energy transport and the control of Arctic summer sea-ice extent. *Nature Climate Change*, 3:744–748, 08 2013. doi: 10.1038/nclimate1884.

J. E. Kay, C. Deser, A. Phillips, A. Mai, C. Hannay, G. Strand, J. M. Arblaster, S. C. Bates, G. Danabasoglu, J. Edwards, M. Holland, P. Kushner, J.-F. Lamarque, D. Lawrence, K. Lindsay, A. Middleton, E. Munoz, R. Neale, K. Oleson, L. Polvani, and M. Vertenstein. The Community Earth System Model (CESM) Large Ensemble project: A community resource for studying climate change in the presence of internal climate variability. *Bull. Amer. Meteor. Soc.*, 96(8):1333–1349, 2015. doi: 10.1175/bams-d-13-00255.1. URL http://dx.doi.org/10.1175/BAMS-D-13-00255.1.

Jennifer E. Kay, Marika M. Holland, Cecilia M. Bitz, Edward Blanchard-Wrigglesworth, Andrew Gettelman, Andrew Conley, and David Bailey. The influence of local feedbacks and northward heat transport on the equilibrium Arctic climate response to increased greenhouse gas forcing. *Journal of Climate*, 25(16):5433–5450, 2012. doi: 10.1175/JCLI-D-11-00622.1. URL https://doi.org/10.1175/JCLI-D-11-00622.1.

Shinya Kobayashi, Yukinari Ota, Yayoi Harada, Ayataka Ebita, Masami Moriya, Hirokatsu Onoda, Kazutoshi Onogi, Hirotaka Kamahori, Chiaki Kobayashi, Hirokazu Endo, Kengo Miyaoka, and Kiyotoshi Takahashi. The JRA-55 reanalysis: General specifications and basic characteristics. *Journal of the Meteorological Society of Japan. Ser. II*, 93(1):5–48, 2015. doi: 10.2151/jmsj.2015-001.

Torben Koenigk and Laurent Brodeau. Ocean heat transport into the Arctic in the twentieth and twenty-first century in EC-Earth. *Climate Dynamics*, 42(11): 3101–3120, Jun 2014. ISSN 1432-0894. doi: 10.1007/s00382-013-1821-x. URL https://doi.org/10.1007/s00382-013-1821-x.

Jean-François Lamarque, G. Page Kyle, Malte Meinshausen, Keywan Riahi, Steven J. Smith, Detlef P. van Vuuren, Andrew J. Conley, and Francis Vitt. Global and regional evolution of short-lived radiatively-active gases and aerosols in the representative concentration pathways. *Climatic Change*, 109(1):191, Aug 2011. ISSN 1573-1480. doi: 10.1007/s10584-011-0155-0. URL https://doi.org/10.1007/s10584-011-0155-0.

Irina Mahlstein and Reto Knutti. Ocean heat transport as a cause for model uncertainty in projected Arctic warming. *Journal of Climate*, 24(5):1451–1460, 2011. doi: 10.1175/2010JCLI3713.1. URL https://doi.org/10.1175/2010JCLI3713.1.

Malte Meinshausen, Steven J Smith, K Calvin, John S Daniel, MLT Kainuma, Jean-Francois Lamarque, Km Matsumoto, SA Montzka, SCB Raper, K Riahi, et al. The RCP greenhouse gas concentrations and their extensions from 1765 to 2300. *Climatic change*, 109(1-2):213, 2011.

Aleksi Nummelin, Camille Li, and Paul J. Hezel. Connecting ocean heat transport changes from the midlatitudes to the Arctic Ocean. *Geophysical Research Letters*, 44(4):1899–1908, 2017. ISSN 1944-8007. doi: 10.1002/2016GL071333. URL http://dx.doi.org/10.1002/2016GL071333. 2016GL071333.

Dylan Oldenburg, Kyle C. Armour, LuAnne Thompson, and Cecilia M. Bitz. Distinct mechanisms of ocean heat transport into the Arctic under internal variability and climate change. *Geophysical Research Letters*, 45(15):7692–7700, 2018. doi: 10.1029/2018GL078719. URL https://agupubs.onlinelibrary.wiley.com/doi/abs/10.1029/2018GL078719.

J. P. Peixoto and A. H. Oort. *Physics of Climate*. American Institute of Physics, 1992.

Donald K. Perovich, Bonnie Light, Hajo Eicken, Kathleen F. Jones, Kay Runciman, and Son V. Nghiem. Increasing solar heating of the Arctic Ocean and adjacent seas, 1979–2005: Attribution and role in the ice-albedo feedback. *Geophysical Research Letters*, 34(19), 2007. doi: 10.1029/2007GL031480. URL https://agupubs.onlinelibrary.wiley.com/doi/abs/10.1029/2007GL031480.

N. A. Rayner, D. E. Parker, E. B. Horton, C. K. Folland, L. V. Alexander, D. P. Rowell, E. C. Kent, and A Kaplan. Global analyses of sea surface temperature, sea ice, and night marine air temperature since the late nineteenth century. *J. Geophys. Res.*, 108(D14), 2003. doi: 10.1029/2002jd002670.

J. A. Screen, C. Deser, and I. Simmonds. Local and remote controls on observed Arctic warming. *Geophysical Research Letters*, 39(10), 2012. doi: 10.1029/2012GL051598. URL https://agupubs.onlinelibrary.wiley.com/doi/abs/10.1029/2012GL051598.

James A. Screen and Ian Simmonds. The central role of diminishing sea ice in recent Arctic temperature amplification. *Nature*, 464:1334 EP –, 04 2010. URL https://doi.org/10.1038/nature09051.

James A. Screen, Clara Deser, Ian Simmonds, and Robert Tomas. Atmospheric impacts of Arctic sea-ice loss, 1979–2009: separating forced change from atmospheric internal variability. *Climate Dynamics*, 43(1):333–344, Jul 2014. ISSN 1432-0894. doi: 10.1007/s00382-013-1830-9. URL https://doi.org/10.1007/s00382-013-1830-9.

Mark C. Serreze and Julienne Stroeve. Arctic sea ice trends, variability and implications for seasonal ice forecasting. *Philosophical Transactions of the Royal Society A: Mathematical, Physical and Engineering Sciences*, 373(2045):20140159, 2015. doi: 10.1098/rsta.2014.0159. URL https://royalsocietypublishing.org/doi/abs/10.1098/rsta.2014.0159.

H. A. Singh, P. J. Rasch, and B. E. J. Rose. Increased ocean heat convergence into the high latitudes with CO2 doubling enhances polar-amplified warming. *Geophysical Research Letters*, 44(20):10,583–10,591, 2017. doi: 10.1002/2017GL074561. URL https://agupubs.onlinelibrary.wiley.com/doi/abs/10.1002/2017GL074561.

Lantao Sun, Clara Deser, and Robert A. Tomas. Mechanisms of stratospheric and tropospheric circulation response to projected Arctic sea ice loss. *Journal of Climate*, 28(19):7824–7845, 2015. doi: 10.1175/JCLI-D-15-0169.1. URL https://doi.org/10.1175/JCLI-D-15-0169.1.

K. E. Taylor, R. J. Stouffer, and G. A. Meehl. An overview of CMIP5 and the experiment design. *Bulletin of the American Meteorological Society*, 93:485–498, 2012.

Kevin E. Trenberth and Julie M. Caron. Estimates of meridional atmosphere and ocean heat transports. *Journal of Climate*, 14(16):3433–3443, 2001. doi: 10.1175/1520-0442(2001)014<3433:EOMAAO>2.0.CO;2.

Takamasa Tsubouchi, Sheldon Bacon, Yevgeny Aksenov, Alberto C. Naveira Garabato, Agnieszka Beszczynska-Möller, Edmond Hansen, Laura de Steur, Beth Curry, and Craig M. Lee. The Arctic Ocean seasonal cycles of heat and freshwater fluxes: Observation-based inverse estimates. *Journal of Physical Oceanography*, 48(9):2029–2055, 2018. doi: 10.1175/JPO-D-17-0239.1. URL https://doi.org/10.1175/JPO-D-17-0239.1.

Geoffrey K. Vallis and Riccardo Farneti. Meridional energy transport in the coupled atmosphere–ocean system: scaling and numerical experiments. *Quarterly Journal of the Royal Meteorological Society*, 135(644):1643–1660, 2009. ISSN 1477-870X. doi: 10.1002/qj.498. URL http://dx.doi.org/10.1002/qj.498.

Justin J. Wettstein and Clara Deser. Internal variability in projections of twenty-first-century Arctic sea ice loss: Role of the large-scale atmospheric circulation. *Journal of Climate*, 27(2):527–550, 2014. doi: 10.1175/JCLI-D-12-00839.1. URL https://doi.org/10.1175/JCLI-D-12-00839.1.

Carl Wunsch. The total meridional heat flux and its oceanic and atmospheric partition. *Journal of Climate*, 18(21):4374–4380, 2005. doi: 10.1175/JCLI3539.1. URL https://doi.org/10.1175/JCLI3539.1.

Haijun Yang, Qing Li, Kun Wang, Yu Sun, and Daoxun Sun. Decomposing the meridional heat transport in the climate system. *Climate Dynamics*, 44(9): 2751–2768, May 2015. ISSN 1432-0894. doi: 10.1007/s00382-014-2380-5. URL https://doi.org/10.1007/s00382-014-2380-5.

Stephen G. Yeager, Alicia R. Karspeck, and Gokhan Danabasoglu. Predicted slowdown in the rate of Atlantic sea ice loss. *Geophysical Research Letters*, 42(24):10,704–10,713, 2015. doi: 10.1002/2015GL065364. URL https://agupubs.onlinelibrary.wiley.com/doi/abs/10.1002/2015GL065364.

Masakazu Yoshimori, Ayako Abe-Ouchi, and Alexandre Laîné. The role of atmospheric heat transport and regional feedbacks in the Arctic warming at equilibrium. *Climate Dynamics*, 49(9):3457–3472, Nov 2017. ISSN 1432-0894. doi: 10.1007/s00382-017-3523-2. URL https://doi.org/10.1007/s00382-017-3523-2.

Rong Zhang. Mechanisms for low-frequency variability of summer Arctic sea ice extent. *Proceedings of the National Academy of Sciences*, 112(15):4570–4575, 2015. ISSN 0027-8424. doi: 10.1073/pnas.1422296112. URL https://www.pnas.org/content/112/15/4570.